Accurate machine-learning predictions of coercivity in high-performance permanent magnets

Churna Bhandari,[1,*] Gavin N. Nop,[1,2] Jonathan D.H. Smith,[1,2] and Durga Paudyal[1,3]

[1] *The Ames National Laboratory, U.S. Department of Energy, Iowa State University, Ames, Iowa 50011, USA*
[2] *Department of Mathematics, Iowa State University, Ames, Iowa 50011, USA*
[3] *Department of Electrical and Computer Engineering, Iowa State University, Ames, Iowa 50011, USA*

(Received 29 February 2024; revised 22 May 2024; accepted 25 July 2024; published 16 August 2024)

Increased demand for high-performance permanent magnets in the electric vehicle and wind-turbine industries has prompted the search for cost-effective alternatives. Discovering magnetic materials with the desired intrinsic and extrinsic permanent magnet properties presents a significant challenge to researchers because of issues with the global supply of rare-earth elements, material stability, and a low maximum magnetic energy product $BH_{\max}$. While first-principles density functional theory (DFT) predicts materials' magnetic moments, magnetocrystalline anisotropy constants, and exchange interactions, it cannot compute extrinsic properties such as coercivity (H_c). Although it is possible to calculate H_c theoretically with micromagnetic simulations, the predicted value is larger than the experiment by almost an order of magnitude due to the Brown paradox. To circumvent these issues, we employ machine-learning (ML) methods on an extensive database obtained from experiments, DFT calculations, and micromagnetic modeling. The use of a large experimental dataset enables realistic H_c predictions for materials such as Ce-doped $Nd_2Fe_{14}B$, comparing favorably against micromagnetically simulated coercivities. Remarkably, our ML model accurately identifies uniaxial magneto-crystalline anisotropy as the primary contributor to H_c. With DFT calculations, we predict the Nd-site-dependent magnetic anisotropy behavior in $Nd_2Fe_{14}B$, confirming that Nd $4g$ sites mainly contribute to uniaxial magnetocrystalline anisotropy, and also calculate the Curie temperature (T_c). Both calculated results are in good agreement with the experiments. The coupled experimental dataset and ML modeling with DFT input predict H_c with far greater accuracy and speed than was previously possible using micromagnetic modeling. Further, we reverse engineer the grain-boundary and intergrain exchange coupling with micromagnetic simulations by employing the ML predictions.

DOI: 10.1103/PhysRevApplied.22.024046

I. INTRODUCTION

With the rapid advance of computational capabilities, there is considerable research interest in machine-learning (ML) methods for predicting material properties using extensive databases [1,2]. Of specific interest is the remarkable speed of these techniques, which outperform traditional first-principles methods like density functional theory (DFT) by an order of magnitude. ML methods can deal with complex structures and are desirable for discovering high-performance permanent magnet materials much needed for the electric vehicle and wind turbine industries. Although recent advances in first-principle methods such as DFT have enabled successful prediction of intrinsic properties, e.g., magnetic moments, magnetocrystalline anisotropy, and exchange interactions, the prediction of coercivity (H_c) is a daunting task. Theoretically, H_c can be computed by solving the phenomenological Landau-Lifshitz-Gilbert equation (LLGE) with micromagnetic simulations, but these simulations overestimate the experimental H_c by an order of magnitude due to the Brown paradox [3–5]. Previous papers employing ML to predict the extrinsic properties [6–9] have been limited exclusively to micromagnetically simulated materials.

ML requires datasets that include information about material properties such as crystal structure, micromagnetic grain size and boundaries, saturation magnetization (M_s), the uniaxial magnetocrystalline anisotropy constant (K_u), the exchange stiffness constant (A_{ex}), and the Curie temperature (T_{c}). To build predictive models based on our dataset, we utilize classical ML and artificial neural network (ANN) algorithms [10–12]. These models establish patterns and relationships between the independent and dependent (H_c) material properties. They are trained on subsets of the known data and tested on the complementary subsets to assess model accuracy and reliability.

---

[*] Contact author: cbb@ameslab.gov

An extensive survey of the literature resulted in a dataset of 300 experimentally known materials (see Appendix B, Table XIII), to our knowledge, the largest current experimental ML magnetic dataset. Our second dataset consists of 8770 micromagnetically computed permanent magnet materials. Various predictive techniques, including ML, statistical inference, and micromagnetic modeling (mumax^3 program) are applied to both datasets to predict and compare H_c [13,14]. In experimental materials, we find standard nonlinear models such as the decision tree (DT), extreme gradient boosting (XGB), and random forest (RF) [15] produce excellent results with $R^2 \sim 0.87$ (where R^2 is a standard statistical measure of accuracy in regression), but tuning the XGB regressor improves the R^2 measure to 0.89. Of note, ML clearly demonstrates that H_c is related directly to K_u, weakly to A_{ex}, and inversely to M_s.

We predict the H_c of cerium (Ce)-doped $\mathrm{Nd_2Fe_{14}B}$ 2:14:1 to demonstrate the complete pipeline enabled by the ML toolkit coupled with *ab initio* calculations. First, for a pure neomagnet, the site contribution to magnetocrystalline anisotropy is analyzed with DFT calculations showing that $4g$ sites mainly contribute to the uniaxial magnetocrystalline anisotropy. Second, our computed T_{C} for a pure compound using Green's function in the atomic sphere approximation (ASA) is in good agreement with the experiment. Finally, we employ DFT-computed parameters in ML for predicting the H_c of Ce-doped compositions. The ML-predicted H_c matches with the experiment, demonstrating that the *ab initio* computed input parameters and the ML methodology are sufficient to predict experimental H_c, even without access to experimental conditions and advanced internal structural properties. Conversely, the ML prediction for selected candidate materials is used to engineer their grain boundary size (GBS) and intergrain coupling.

II. MICROMAGNETISM

Micromagnetics is the study of the behavior of magnetic materials, typically in the nanometer range. During its early formulation [16,17], the field emphasized qualitative aspects of magnetism: the role of domain structures, domain walls, and magnetic vortices in ferromagnetic materials. The transition to computer simulation in micromagnetics was a significant advance, providing a detailed examination of the forces at play inside a magnetic material [18].

Naively, the estimate $2K_u/M_s$ gives an upper bound on H_c [3,19]. However, this estimate disregards impurities and multigrain structures in materials, leading to a gross overestimate of H_c from theory alone: the Brown paradox. Micromagnetic simulations, which include demagnetization (shape anisotropy), are crucial for a good understanding of magnetic materials, but the interplay among these complex effects and the Brown paradox still hinder accurate predictions of H_c.

A. Theory

Magnetodynamics is described by a nonlinear partial differential equation for the spatio-temporal magnetization vector $\mathbf{M}(\mathbf{r},t)$. The time evolution of $\mathbf{M}(\mathbf{r},t)$ is given by a phenomenological Landau-Lifshitz-Gilbert (LLG) equation [16,17]

$$\begin{aligned}\frac{\partial \mathbf{M}(\mathbf{r},t)}{\partial t} &= \frac{\gamma}{1+\alpha^2}\mathbf{M}(\mathbf{r},t)\times\mathbf{H}_{\mathrm{eff}}(\mathbf{r},t)\\ &\quad-\frac{\alpha\gamma}{1+\alpha^2}\mathbf{M}(\mathbf{r},t)\times\left[\mathbf{M}(\mathbf{r},t)\times\mathbf{H}_{\mathrm{eff}}(\mathbf{r},t)\right].\end{aligned} \tag{1}$$

Here, $\mathbf{M}(\mathbf{r},t)$ is the unit vector describing the magnetization of the material with M_s as the saturation magnetic moment per unit volume, while $\mathbf{H}_{\mathrm{eff}}(\mathbf{r},t)$, γ, and α, respectively, are the effective static magnetic field, the gyromagnetic ratio, and the damping parameter (quantifying the rate at which the magnetization relaxes back to equilibrium). In Eq. (1), the first term is the precession of the magnetic moment around the external magnetic field. The second term is the damping, which relaxes the magnetic moment to the equilibrium. For time-independent scenarios, such as the computation of a hysteresis loop, the α term is set to 0. Then, $\mathbf{H}_{\mathrm{eff}} = \mathbf{H} + \mathbf{H}_{\mathrm{ms}} + \mathbf{H}_{\mathrm{ex}} + \mathbf{H}_a$. The terms are as follows. $\mathbf{H}$ is the externally applied field, which is taken as a parameter. $\mathbf{H}_{\mathrm{ms}}$ is a long-range magnetic field

$$\mathbf{H}_{\mathrm{ms}}(\mathbf{r}) = \frac{1}{4\pi}\int \nabla\nabla' \frac{1}{|\mathbf{r}-\mathbf{r}'|}\cdot M(\mathbf{r}')dr' \tag{2}$$

corresponding to self-interaction of the induced magnetic field with the magnetization across the material [20]. The exchange field is the Laplacian of the magnetization, which is obtained from the classical Heisenberg model

$$\mathbf{H}_{\mathrm{ex}} = \frac{2A_{\mathrm{ex}}}{M_s}\nabla\mathbf{M}(\mathbf{r},t). \tag{3}$$

Although this expression was originally deduced for localized spins, it is still valid for itinerant systems to the first-order approximation. A_{ex} is a measure of the strength of magnetic exchange interaction. H_a is the uniaxial anisotropy term, written as

$$\mathbf{H}_a = \frac{2K_{u1}}{M_s}\left(\mathbf{u}\cdot\mathbf{M}(\mathbf{r},t)\right)\mathbf{u} + \frac{2K_{u2}}{M_s}\left(\mathbf{u}\cdot\mathbf{M}(\mathbf{r},t)\right)^3\mathbf{u}, \tag{4}$$

where K_{u1} and K_{u2} are anisotropy constants, and u indicates the direction of the anisotropy vector, making it easier for the magnetization to align with the direction of u in the case of ferromagnetic materials. Most papers envisage only a single constant: $K_{u1} = K_u$ and $K_{u2} = 0$. Other terms, such as the Dzyaloshinskii-Moriya interaction (DMI), were neglected due to the lack of experimental data for current materials and the relatively weak effect in modern magnetic materials [21].

In order to estimate fundamental magnetic parameters in cases of partial experimental information, the following relations were utilized. $A_{\rm ex}$ is inversely proportional to the lattice constant (a) as given by

$$A_{\rm ex} = \frac{JS^2}{a} n, \tag{5}$$

where S is the spin quantum number, and n is the number of magnetic ions per unit cell. Equivalently, $A_{\rm ex}$ can be expressed approximately in terms of $T_{\rm C}$ as

$$A_{\rm ex} \sim \frac{3T_{\rm C}}{2za}. \tag{6}$$

Here z is the number of the nearest neighbors of a magnetic ion. Finally, the equation

$$BH_{\rm max} = \frac{\mu_0 M_s^2}{4} \tag{7}$$

is used to estimate M_s from the vacuum permeability μ_0 and the maximum energy product $BH_{\rm max}$, which is given by the maximum product of the magnetic flux density and the magnetic field strength at any point on the hysteresis loop [22].

The micromagnetic equations are solved in the continuum approximation $\mathbf{M}(\mathbf{r}, t) = M_s(r)\mathbf{m}(\mathbf{r}, t)$ [23–25]. $\mathbf{H}_{\rm eff}$ is deduced from the magnetic free energy functional $F[\mathbf{m}]$ as $\mathbf{H}_{\rm eff} = -(1/\mu_0 M_s)\delta F[\mathbf{m}]/\delta \mathbf{m}$;

$$\begin{aligned} F[\mathbf{m}] = \int_V \Big[& A_{\rm ex}(\nabla \mathbf{m})^2 - \mu_0 \mathbf{M}\cdot\mathbf{H}_{\rm ex} - K_u(\mathbf{m}\cdot\mathbf{u})^2 \\ & -\mu_0 \mathbf{M}\cdot\mathbf{H} - \frac{\mu_0}{2}\mathbf{M}\cdot\mathbf{H}_{\rm dem} + f_{\rm DMI}(\mathbf{m}) + \cdots \Big] d^3\mathbf{r}, \end{aligned} \tag{8}$$

where $f_{\rm DMI}$ is DMI. Additional terms may be added as needed to count for additional interactions. The $F[m]$ is minimized with respect to m using the steepest descent algorithm as implemented in the micomagnetic program [25]. Then the hysteresis loop is obtained by evaluating m in each equilibrium magnetic state for different values of the external applied magnetic field.

B. Experimental materials

An experimental database of 300 magnetic materials was assembled [19,26–80]. A material was chosen if K_u, M_s, and H_c were explicitly included in the experimental results. For the $R_2Fe_{14}B$ family (where R is a rare-earth element) and some other materials, only the experimental anisotropy field (H_a) is available, so the estimate $H_c \sim H_a/4$ was used [81].

The exchange strength $A_{\rm ex}$ was determined in one of three different ways. The first was a direct reporting of the stiffness exchange, which was rarely available. For some materials, the value was interpolated from the values for similar alloys and compounds. The third method derived $A_{\rm ex}$ from the Curie-stiffness relation in Eq. (6), using the experimental Curie temperature $T_{\rm C}$ and known lattice constant a [82]. This latter method was used for $R_2Fe_{14}B$, including Ce-doped $Nd_2Fe_{14}B$ [70], binary alloys [68], $SmCo_5$, 1:5 compositions [65], La/Pr/Co-doped hexaferrites [60], and other element-doped hexaferrites [55, 56,59,83].

There was significant variation in the reported H_c values, depending on the experimental conditions and fabrication methods. For example, the atmospheric composition during the annealing of iron (Fe) magnets affected H_c as oxygen modified the material composition during the hardening process. Oxygenated crystalline defects, such as nucleation and pinning of the domain walls, play critical roles in the H_c mechanism. The nucleation field [84] (the magnetic field at which the atomic spin ceases to align along the magnetic easy axis) lowers the measured H_c, while pinning does the opposite.

Cooling rates have significant effects on the material grain size [19,26–80]. Several dozen materials (notably Nd- and Fe-based ferromagnets) have grain sizes recorded in the database. Grain composition, as visualized in Fig. 1, is known to be heavily predictive of a material's H_c [85]. However, correlating the grain measurements from different sources made it apparent that a single number cannot completely represent the grain structure and that the particular measurement techniques employed may induce additional inaccuracies. In any material with multiple measurements for a property, a representative median was selected from a specific experiment (defaulting to papers with more comprehensive material property estimates). This choice was made before applying statistical techniques to ensure that no bias contaminated the dataset.

For the better training of ML networks, an additional database was computed, using micromagnetic modeling with $H_{\rm ms}$, $H_{\rm ex}$, H, $H_{\rm dem}$, and H_a in the $H_{\rm eff}$. $A_{\rm ex}$, K_u, and M_s were supplied as the inputs for stiffness exchange, magnetocrystalline anisotropy, and saturation magnetization. The input parameters were uniformly sampled from the cuboid determined by the ranges of $A_{\rm ex}$, K_u, and M_s in the 300 experimental materials. There are then two measures of H_c: the experimentally measured coercivity H_c(exp), possessed only by the experimental materials, and the computationally determined H_c, calculated for both the hypothetical and the experimental materials.

For micromagnetic modeling, simple structures were chosen for the magnetic samples. Due to the limited

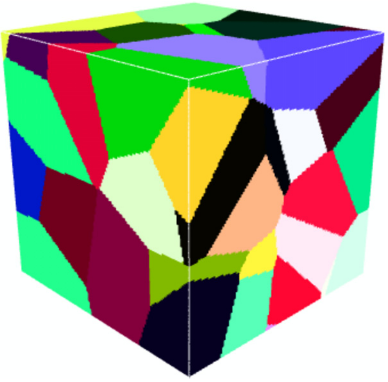

FIG. 1. A magnetic cuboid of size $128 \times 128 \times 128$ nm^3 showing different micromagnetic grains. The colors within each grain refer to different magnetization directions. The snapshot of spin texture is captured during the micromagnetic simulation.

grain-structure data, for the majority of the database, a single structure composed of multiple grains would have been chosen for the materials. This would have induced scaling on the H_c, which instead may be modeled directly with ML. As no grains or boundaries were involved in the computation, a magnetic cube of $32 \times 32 \times 32$ at nm^3 scale was found to be sufficient to avoid loss of precision in the uniform uniaxial anisotropy alignment. For Ce-substituted compositions, we used simulation cells of size $128 \times 128 \times 128$ nm^3 for grain-boundary engineering, as shown in Fig. 1.

C. Micromagnetic results

We compute the H_c for experimentally known systems and list the comparison of the calculated and experimental values for selected materials in Table I. Theoretically, the upper limit for H_c is the anisotropy field [86] $H_a = 2K_u/M_s$; however, the true experimental value is an order of magnitude smaller due to the uncertainty in the coercivity mechanism in permanent magnets, commonly known as the Brown paradox [3]. Experimentally measured H_c values fit well with the empirical Kronmüller equation [87] $H_c = cH_a - N_{\rm eff} 4\pi M_s$ [88,89], where cH_a is the field to nucleate a reverse domain, and $N_{\rm eff} 4\pi M_s$ is the demagnetization field, with c and $N_{\rm eff}$ being renormalization factors. For example, $Nd_2Fe_{14}B$ (sintered) has $c \sim 0.25(0.37)$ and $N_{\rm eff} \sim 0.26(1)$ [88,89].

The micromagnetically simulated H_c values differ from the experimental values by a factor of up to approximately 5. Interestingly, these values are very similar to the experimental H_a. Moreover, for some materials, the use of the estimated values for M_s, $A_{\rm ex}$, and K_u using the empirical relations as discussed in Eqs. (5)–(7) will result in additional error. In general, H_c depends nonlinearly on grain size and domain-wall width or particle size in magnetic materials [85,90–93]. In modern manufacturing, grain sizes are larger relative to domain sizes. This is especially common in neomagnets, leading to a decrease of H_c with increasing grain size [94], where higher grain surface area hosts more defects. Grain-boundary size also affects the demagnetization factor [95], further reducing H_c.

TABLE I. Comparison of calculated and experimental H_c for different rare-earth permanent magnets. For realistic comparisons, the mumax^3 values are scaled by a factor of $c = 0.25$ in column cH_c. The $H_c^{\rm diff}$ column presents the difference between cH_c and $H_c^{\rm exp}$.

Material	$M_s^{\rm exp}$ (MA/m)	$A_{\rm ex}^{\rm exp}$ (pJ/m)	$K_u^{\rm exp}$ (MJ/m^3)	$H_c^{\rm exp}$ (T)	$H_c^{\rm mumax^3}$ (T)	cH_c (T)	$H_c^{\rm diff}$ (T)
$La_2Fe_{14}B$	1.09	7.41	1.4	0.50	2.11	0.53	0.03
$Ce_2Fe_{14}B$	0.93	6.00	1.70	0.54	3.14	0.79	0.25
$Pr_2Fe_{14}B$	1.24	7.94	4.66	1.54	6.46	1.62	0.08
$Nd_2Fe_{14}B$	1.27	8.23	4.65	1.24	6.25	1.56	0.32
$Gd_2Fe_{14}B$	0.71	9.33	0.85	0.23	2.40	0.60	0.37
$Tb_2Fe_{14}B$	0.56	8.78	6.13	2.93	21.62	5.41	2.48
$Dy_2Fe_{14}B$	0.56	9.42	4.24	1.70	14.79	3.70	1.99
$Ho_2Fe_{14}B$	0.64	8.14	2.42	0.75	7.26	1.82	1.07
$Lu_2Fe_{14}B$	0.93	7.66	1.21	0.29	2.30	0.58	0.28
$Y_2Fe_{14}B$	1.12	8.01	1.46	0.19	2.16	0.54	0.35
$Th_2Fe_{14}B$	1.12	6.77	1.46	0.17	2.10	0.53	0.36
$La_2Co_{14}B$	0.79	1.50	1.19	0.34	3.06	0.77	0.42
$Pr_2Co_{14}B$	1.04	1.51	5.20	2.50	9.43	2.36	−0.14
$Nd_2Co_{14}B$	1.08	1.51	2.42	3.69	4.22	1.05	−2.64
$Gd_2Co_{14}B$	0.23	1.52	1.03	0.30	9.48	2.37	2.07
$Y_2Co_{14}B$	0.85	1.52	1.19	0.34	2.84	0.71	0.37
$SmCo_5$	0.86	1.20	1.72	7.50	38.80	9.70	2.20
YCo_5	0.78	7.11	5.50	3.90	13.33	3.33	−0.57
$LaCo_5$	0.71	6.47	6.30	5.25	16.89	4.22	−1.03
$CeCo_5$	0.60	5.13	6.40	5.70	20.66	5.17	0.57
$PrCo_5$	0.94	6.96	8.10	5.32	16.08	4.02	−1.30
$NdCo_5$	0.93	7.09	0.24	0.15	0.47	0.12	−0.03

The experimental features for 211 of the 300 materials in the dataset are known, while the remaining 90 materials require the use of the aforementioned theoretical models to determine A_{ex} from experimental results. These materials show larger discrepancies in the micromagnetically predicted H_c, which is worth investigating both experimentally and theoretically. We show a comparison of these results (for selected key magnetic materials) in Table I. As all micromagnetically predicted H_c values are overestimated, the only meaningful comparison is obtained with a scaled coercivity cH_c, which for $c = 0.25$ fits well with the experimental values obtained for the 210 materials. The cH_c estimate is generally a good match for 2:14:1 compositions, except for Co-based $Nd_2Co_{14}B$ and $Gd_2Co_{14}B$. However, the appropriate scaling factor may vary for different compositions. Overall, the H_c variation with independent features is similar in both theory and experiment, although there are some exceptions such as $La_2Fe_{14}B$. For 1:5 compositions, a similar trend is evident.

III. MACHINE LEARNING

A. Classical machine-learning algorithms

Machine learning encompasses a variety of advanced statistical techniques. It creates a correspondence between a space of independent variables, X, and a space of dependent variables, Y, by taking a ground truth function $f_o : X_o \rightarrow Y$ representing a sequence of observations on a limited subset $X_o \subset X$ of the data to construct a more general function $f : X \rightarrow Y$, which extends the function f_o. This ground truth function may also be represented as a list of observations $\{x_i \mapsto y_i\}_i \subset X_o \times Y$. The method by which f is constructed from f_o is referred to as ML, and it is written symbolically as $f = \text{ML}(f_o) = \text{ML}(\{x_i \mapsto y_i\}_i)$, where ML is optionally subscripted to indicate the algorithm or hyperparameters in use.

The goal of ML is to represent the structure underlying f_o as f. This is usually quantified by splitting the observations into a training set f_o' and testing set f_o^* so that $f_o' \cap f_o^* = \emptyset$. Then the function is constructed relative to a norm, termed a loss function, so that $||f_o' - \text{ML}(f_o')||$ is minimized in some appropriately defined subspace of $X \rightarrow Y$ to avoid overfitting. The quality of the fit with $f = \text{ML}(f_o')$ is measured by evaluating $||f_o^* - f||$ using the same class of norms. In this paper, all ML algorithms use the standard Euclidean norm.

We use the `scikit-learn` library for the Python programming language for predictive data analysis [96]. The dataset (both experimental and theoretical) is split into a 70:30 train-to-test dataset ratio for the model training. Performance does not change drastically by modifying the split ratio to 80:20. The classical linear ML models used are as follows:

1. Linear regression.
2. Lasso regularization.
3. Ridge regularization.

The nonlinear classical ML models used are as follows:

1. Decision-tree (DT) regression.
2. Random-forest (RF) regression.
3. Gradient-boost (GB) regression.
4. XGBoost (XGB) regression.

In ML training with cross-validation, the training dataset is further divided into two parts—the training and the validation datasets. Most ML models have arbitrary hyperparameters, which are not modified directly during training. The validation dataset allows a metatraining of the ML models by random or grid search on the training data and evaluation on the validation set without contaminating the testing set by predicting an ML hyperparameter choice for test set evaluation. The most relevant cross-validation method is k-fold validation. The dataset is randomly split into k disjoint subsets, then one set is chosen as the validation dataset, while the others are chosen as training datasets.

B. Artificial neural networks

An artificial neural network (ANN) is suitable for high complexity problems such as H_c prediction. Figure 2 shows a schematic diagram (a portion used in the calculations) for an ANN consisting of an input layer (six neurons), two hidden layers (containing four and three neurons, respectively), and the output layer with one neuron. A nonlinear activation function `leaky-relu` [$f(z) = \max(0, z) + 0.01 * \min(0, z)$] is used between the input and hidden layers to counter typical convergence problems found in small ANNs. We used the state-of-the-art gradient-descent benchmark optimizer Adam [97], as implemented in `tensorflow` [98] in the Keras API [99].

C. Performance comparison

For the regression model, given an ML fit, we use two common statistical measures of error applied to the H_c predictions: (i) mean square error (MSE):

$$\text{MSE} = \frac{1}{N}\sum_{i}^{N}(y_i - y_{\text{pred}_i})^2, \tag{9}$$

which is also used for training all ML models, and (ii) R squared (R^2):

$$R^2 = 1 - \frac{\text{MSE}}{V(y)}, \tag{10}$$

where $V(y)$ is the variance written as

$$V(y) = \langle (y_i - \langle y \rangle)^2 \rangle \tag{11}$$

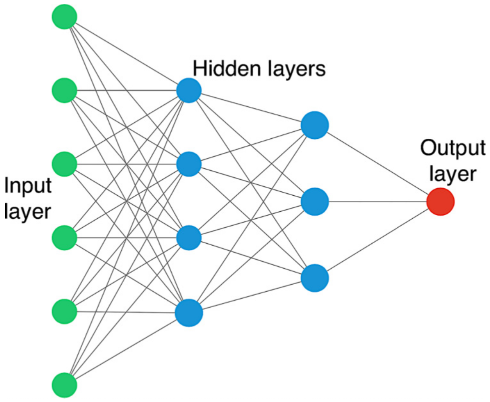

FIG. 2. Schematic diagram showing an artificial neural network (only a portion used in the calculations) with six neurons in the input layer, four and three neurons in the second and the third deep (hidden) layers, and a neuron for regression in the output layer. Two different ANN's were used in actual calculations, as discussed in the main text.

with $\langle y\rangle$ as the mean of the predicted values. Equivalently, we may write $R^2 = 1 - \mathrm{RSS}/\mathrm{TSS}$, where RSS is the residual sum of squares $\mathrm{RSS} = \sum_i^N (y_i - y_{\mathrm{pred}_i})^2$, and TSS is the total sum of squares $\mathrm{TSS} = \sum_i^N (y_i - \langle y\rangle)^2$. The loss function is usually written as a sum of the MSE and the first- or second-order norms of the target function parameters. This provides convergence of the model and penalizes overfitting for parameterized machine learning.

D. Results and discussion

1. Machine learning on experimental data

Here, we explore the experimental data and the relation between target and independent variables. Figure 3 visualizes H_c as a function of K_u, M_s, and A_{ex}. The actual values of the variables differ by several orders of magnitude. They are scaled using the `sci-kit minmaxscalar` in which a dimensionless scaled feature variable x_{scaled} in the range [0, 1] is obtained using the following relation:

$$x_{\mathrm{scaled}} = \frac{(x - x_{\min})}{(x_{\max} - x_{\min})}, \tag{12}$$

where $x_{\min}$ and $x_{\max}$ are minimum and maximum values of the feature variable x. Figure 3 shows an increase of H_c with K_u, a decrease with M_s, and very little variation with A_{ex}.

In gradient-based algorithms, such as ANN, additive relationships are easier to model than multiplicative ones, so the independent and dependent variables are logarithmically scaled. Accordingly, the measures of model performance are given in terms of the logarithm of the H_c. As a result of this change, the absolute measure of R^2 is increased by approximately 0.01 for all gradient-based models.

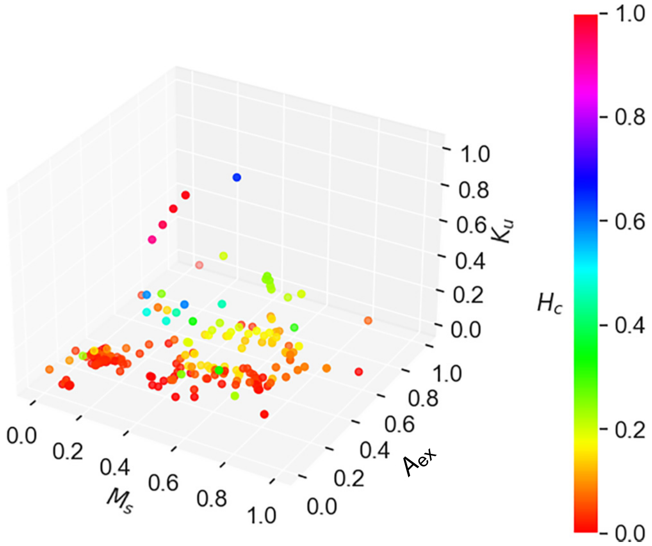

FIG. 3. The distribution of H_c as a function of M_s, A_{ex}, and K_u in experimental magnetic materials. The physical quantities are rendered as normalized and dimensionless. The color map shows the magnitude of H_c.

Figure 4 shows a comparison of ML and experimental H_c for the test dataset. The XGB-tuned model shows better performance than ANN Adam. Table II shows the performance of various ML models. The linear models show poor performance, with $R^2 \ll 1$. This demonstrates the complex nonlinear relation between the dependent and independent variables. The nonlinear models DT, XGB, and RF perform better, with R^2 values of 0.89, 0.87, and 0.87, respectively. These values still witness a decrease from the R^2 scores of more than 0.9 on the training dataset.

The ANN model has R^2 scores that are similar to other classical models (see Table II). The ANN architecture using dense layers = 64, activation function = leaky_relu, dense layers = 32, activation function = leaky_relu, dense layers = 16, activation function = leaky_relu, and output layer = 1, and learning rate = 0.007, epochs = 1000, batch size = 24, showed similar R^2 scores to RF. This weak performance for the ANN architecture is attributed to the smallness of the dataset size.

a. Feature importance. The model performance can be further validated from the dependence of H_c on the independent features. We compute the importance of RF features by utilizing the model-agnostic interpretive features of `scikit-learn` on the RF and XGB regression models [100]. The feature importance is computed by the Gini index

$$\text{Gini index} = 1 - \sum_i p_i^2, \tag{13}$$

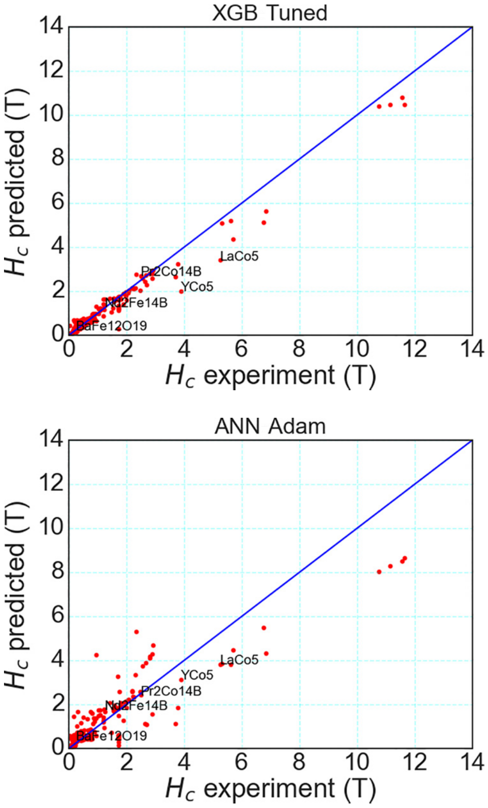

FIG. 4. ML predicted and experimental coercivities of magnetic materials obtained with tuned XGB (top) and ANN (bottom). Selected key materials are labeled in the figure. Nonlinear regressors all yield similar results.

where p_i is the probability of class i in the data. Figure 5 depicts the relative importance of the independent parameters for H_c, as computed by the XGB model. ML accurately identifies K_u as the leading contributing feature to H_c. More surprisingly, the effect of M_s is about 4 times smaller than that of K_u. The uneven distribution of magnetic materials (shown in Fig. 3), and a constant noise level, may explain the unequal weighting of K_u and M_s. Finally, we note that A_{ex} has a comparatively minimal effect on H_c.

2. Machine-learning prediction from micromagnetic data

In order to explore the relation between H_c and the independent variables, we used 8770 micromagnetic simulation-generated data points as a training set. The correlation between variables is given by Pearson's correlation coefficient, which is defined as

$$r = \frac{\sum(X_1 - \langle X_1\rangle)(X_2 - \langle X_2\rangle)}{\sqrt{\sum(X_1 - \langle X_1\rangle)^2 \sum(X_2 - \langle X_2\rangle)^2}}, \tag{14}$$

TABLE II. Comparison of R^2 and mean squared error (MSE) metrics in different ML models on test datasets for experimental materials. The nonlinear regression models show better values of R^2 and MSE than the linear models. The error is evaluated over the difference of the logarithm of the coercivity in T.

Model	R^2	MSE
Linear regression	0.62	0.64
Lasso	0.38	1.07
Ridge	0.63	0.64
Lasso-CV	0.61	0.68
Ridge-CV	0.63	0.66
Elasticnet	0.62	0.66
DT regressor	0.89	0.19
DT pruned	0.84	0.27
RF regressor	0.87	0.23
Gradient-boosting regressor	0.80	0.34
Tuned gradient boosting (GB) regressor	0.87	0.22
XGB regressor	0.87	0.23
Tuned XGB regressor	0.89	0.18
ANN (Adam)	0.64	0.62
Light gradient boosted machine (LGBM)	0.70	0.60
Fine-tuned ANN	0.85	0.25

where X_i and $\langle X_i\rangle$ denote the variable i and its average value. A positive (or negative) value of r indicates a positive (or negative) correlation between the two variables: the higher the r value, the higher the correlation. Figure 6 shows a correlation heatmap for the variables. The distribution for the 8770 dataset is right skewed, as shown in Fig. 7, with a peak around 0.2–0.4 T. It is similar to the distribution for the experimental materials (not shown here): most of the materials have values around the peak, and a few materials, such as 1:5 compositions, have larger values of 2–6 T. For better ML training, logarithmic transformation is appropriate for skewed data, which is employed in our model fits.

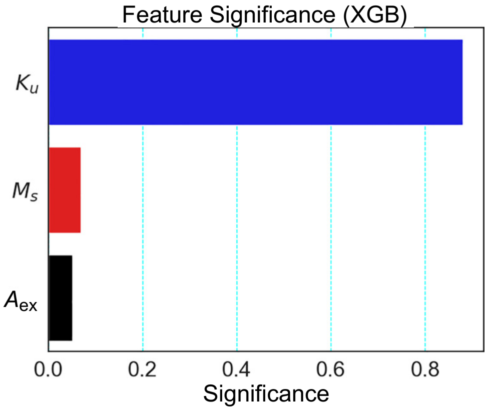

FIG. 5. Histogram of key features contributing to H_c in the XGB model. The K_u clearly leads, followed distantly by M_s and A_{ex}.

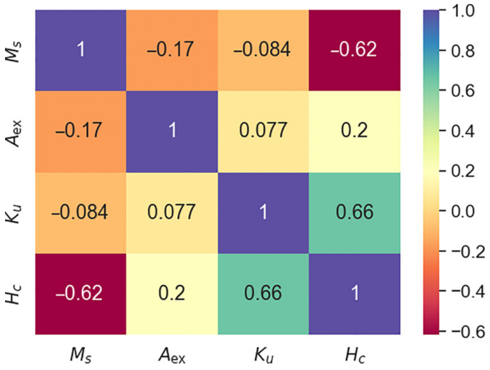

FIG. 6. Heat map showing the correlation between the H_c, A_{ex}, K_u, and H_c. The color palette corresponds to the correlations between the variables. H_c is strongly correlated with K_u, negatively correlated with M_s, and weakly correlated with A_{ex}. M_s shows a slightly negative correlation with K_u and A_{ex}. K_u shows a slightly positive correlation with A_{ex}.

TABLE III. mumax^3 data on hypothetical materials: Comparison of R^2 and MSE of H_c for different ML models. All the errors are evaluated over the ln of the H_c in T. The fine-tuned model hyperparameters are given in Appendix A.

Model	R^2	MSE
Linear regression	0.95	0.22
Lasso	0.54	2.13
Ridge	0.95	0.22
Lasso-cv	0.95	0.25
Ridge-cv	0.95	0.22
Elasticnet	0.94	0.26
DT regressor	0.97	0.13
DT pruned	0.97	0.15
RF regressor	0.98	0.08
GB regressor	0.98	0.09
Tuned GB regressor	0.98	0.08
XGB regressor	0.98	0.09
Tuned XGB regressor	0.98	0.08
ANN	0.98	0.09

Significantly, the strongest (absolute) correlation is observed between H_c and K_u at 0.66, followed by M_s with a correlation of -0.62, and then by A_{ex} at 0.2. This pattern suggests a high dependence of H_c on K_u. The negative correlation between H_c and M_s aligns with the theoretical relationship $H_c \propto M_s^{-1}$. Similarly, the correlation coefficient (r) between H_c and K_u or A_{ex} validates the proportionalities $H_c \propto K_u$ and $H_c \propto A_{\mathrm{ex}}$. These findings are consistent with the trends observed in actual materials, as illustrated in Fig. 3.

Next, we discuss the model performance in micromagnetic simulation data, as given in Table III. Both linear and nonlinear models perform well, as the R^2 score is above 0.9. This is expected in a linear regression model where multivariate analysis demonstrates very little multicollinearity in randomly generated independent variables. The multicollinearity can be measured with the variance inflation factor (VIF) $\mathrm{VIF}_\alpha = (1 - R_\alpha^2)^{-1}$, where R_α^2 is the R^2 [Eq. (10)] value of H_c considered as a function of variable α. The computed VIF factors are 1.53 for M_s, 4.36 for A_{ex}, and 1.53 for K_u.

More advanced decision-tree regressors improve the performance. XGB, as the most accurate model, was used as a benchmark, with the hyperparameters given in Appendix A for H_c prediction from experimental data. The deviance in the MSE of the training and testing datasets is shown in Fig. 14. ANNs exhibit performance similar to other nonlinear regressors. The ANN is as follows: dense layers = 64, activation function = leaky_relu, dense layers = 32, activation function = leaky_relu, dense layers = 16, activation function = leaky_relu, and output layer = 1, and learning rate = 0.007, epochs = 1000, batch size = 56. To obtain a deeper insight into ML predictability, the experimental, scaled-micromagnetic, and ML-predicted H_c values are compared with only the known important rare-earth-based materials in Table IV. In general,

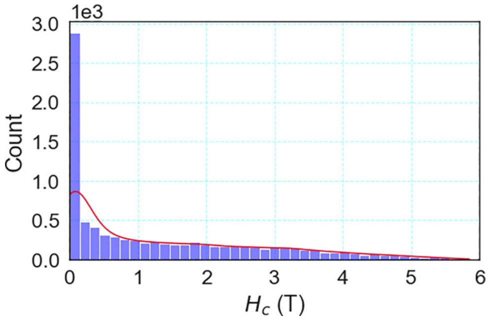

FIG. 7. Distribution of H_c in the training set of 8770 data points. The y axis is scaled by 10^3. The data points are right skewed.

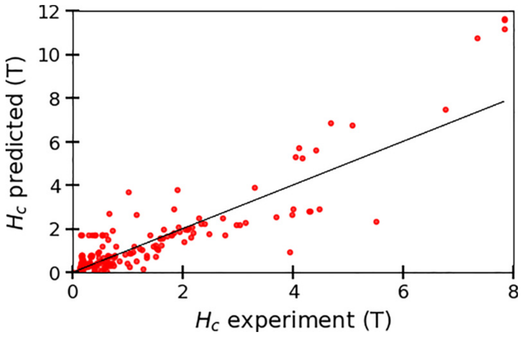

FIG. 8. Scatter plot showing the comparison of experimental and ML-mumax^3 (ML-micromagntics data) predicted H_c for experimental materials.

TABLE IV. H_c (in T) comparisons among experiment, ML prediction, and scaled mumax^3 for different permanent magnetic materials. The ML (tuned XGB and ANN) predictions are obtained by training the hypothetical materials using the random independent variables M_s, A_{ex}, and K_u, and the mumax^3 computed H_c. RMSE and MAE quantify the discrepancy between the experimental ML and the mumax^3 scaled cH_c.

Material	H_c(exp)	H_c(XGB)	H_c(ANN)	cH_c
$La_2Fe_{14}B$	0.52	0.52	0.48	0.53
$Ce_2Fe_{14}B$	0.54	0.84	0.73	0.79
$Pr_2Fe_{14}B$	1.54	1.59	1.54	1.62
$Nd_2Fe_{14}B$	1.24	1.50	1.45	1.56
$Gd_2Fe_{14}B$	0.23	0.56	0.52	0.60
$Tb_2Fe_{14}B$	2.93	4.00	5.65	5.41
$Dy_2Fe_{14}B$	1.70	2.76	3.80	3.70
$Ho_2Fe_{14}B$	0.75	1.50	1.76	1.82
$Lu_2Fe_{14}B$	0.29	0.59	0.52	0.58
$Y_2Fe_{14}B$	0.19	0.57	0.48	0.54
$Th_2Fe_{14}B$	0.17	0.56	0.48	0.53
$La_2Co_{14}B$	0.34	0.65	0.68	0.77
$Pr_2Co_{14}B$	2.50	2.28	2.24	2.36
$Nd_2Co_{14}B$	3.69	1.00	0.90	1.06
$Gd_2Co_{14}B$	0.30	0.67	2.79	2.37
$Y_2Co_{14}B$	0.34	0.62	0.61	0.71
$NdLaCeF_{14}B$	0.65	1.33	1.25	1.39
$LaCeYFe_{14}B$	0.41	0.99	1.26	1.39
$NdPrFe_{14}B$	0.80	1.33	1.27	1.39
Sm_2Co_{17}	1.25	1.60	1.53	1.62
$Sm_2Fe_{17}N_3$	2.30	2.46	3.13	2.95
$SmCo_5$	7.50	6.76	6.66	9.70
YCo_5	3.90	2.63	2.68	3.33
$LaCo_5$	5.25	4.18	4.14	4.22
$CeCo_5$	5.70	4.10	5.10	5.17
$PrCo_5$	5.32	4.05	3.81	4.02
$NdCo_5$	0.15	0.12	0.10	0.12
RMSE		0.90	1.10	1.10
MAE		0.68	0.78	0.80

ML-predicted values are smaller than the micromagnetically computed values. For 2:14:1 rare-earth magnets, ML improves the results. For 1:5 rare-earth magnets, it slightly underestimates the experiment. The full comparison of experimental and ML-predicted data is given in Fig. 8

Additionally, XGB was trained with different fractions of the dataset, from 200 to 12 000, by computing the mean absolute error (MAE) error metric:

$$\text{MAE} = \frac{1}{N}\sum_{i=1}^{N}\left|y_i - y_{\text{pred}_i}\right|. \tag{15}$$

Figure 9 shows the convergence of the MAE (obtained with the XGB model) plotted against the training dataset size, indicating that the model performs well for datasets with more than 6000 points.

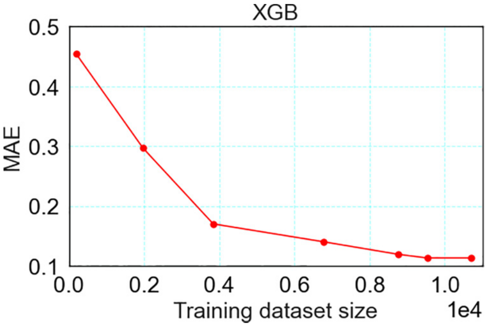

FIG. 9. MAE convergence for H_c with respect to training dataset size in the XGB model. The x axis is in the scale of 10^4.

Next, we discuss the loss function RMSE to examine the model performance. We computed the root mean square error (RMSE) as

$$\text{RMSE} = \sqrt{\frac{1}{N}\sum_{i=1}^{N}(y_i - \hat{y}_i)^2}, \tag{16}$$

where y and $\hat{y}$ refer to the experimental and ML/mumax^3 predicted values. Remarkably, the RMSE and MAE between experimental and ML (tuned XGB) predicted values are smaller than the RMSE and MAE between experimental and the scaled mumax^3 (see Table IV), indicating that ML helps to correct the mumax^3 predictions. It also shows how the H_c is correlated with other features. Moreover, ML is an order of magnitude computationally faster than mumax^3 , and we can use the trained model for predicting H_c in alternative materials without any mumax^3 calculations.

IV. ML APPLICATION WITH DFT

Our computational H_c predictions involve two steps: DFT for Ce-doped $Nd_2Fe_{14}B$, and then ML trained on micromagnetically generated databases with input parameters from the DFT computations.

A. DFT methods and crystal structure

We used the Vienna *ab initio* simulation package (VASP) [101,102] with the projector augmented wave (PAW) formalism in the generalized gradient approximation (GGA) of Perdew-Burke-Ernzerhof (PBE) semilocal exchange-correlation functionals [103,104], including onsite electron-electron correlation Dudarev-Hubbard [105] $U_{\text{eff}} = U - J$ for the $4f$ states of Nd, and spin-orbit interaction. The kinetic energy cutoff is 520 eV for the plane-wave expansion, with a $4 \times 4 \times 2$ $\mathbf{k}$ mesh for the Brillouin zone integration. The experimental structure was used in calculations to avoid overestimating bond lengths and lattice constants in the PBE.

The crystal structure of $Nd_2Fe_{14}B$ is tetragonal with 68 atoms (four formula units), having space group $P42/mnm$ (136) and lattice constants $a = b = 8.80$ and $c = 12.20$

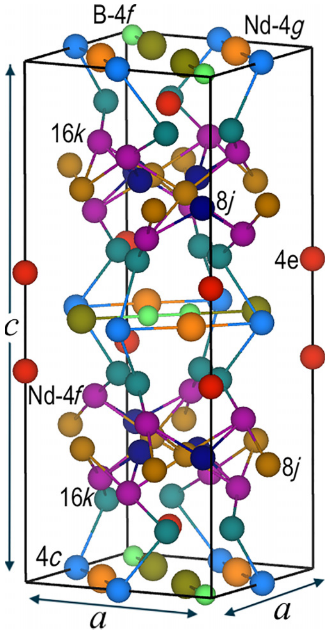

FIG. 10. Crystal structure of $Nd_2Fe_{14}B$ occupied by Nd at two nonequivalent sites $4f$ and $4g$, Fe at six inequivalent sites $16k$, $16k$, $8j$, $8j$, $4c$, and $4e$ (labeled by Wyckoff positions), and B at the $4f$ site.

Å, taking $\alpha = \beta = \gamma = 90^\circ$ at a temperature $T = 285$ K [19,106], with experimental parameters for full Ce-doped $Nd_2Fe_{14}B$ [107]. The crystal structure of the 2:14:1 neomagnet is shown in Fig. 10, which consists of rare-earth Nd in the two inequivalent sites $4f$ and $4g$, transition element Fe in the six inequivalent sites at $16k$, $16k$, $8j$, $8j$, $4e$, and $4c$, and finally B at the $4f$ sites. Fully self-consistent spin-orbit calculations, i.e., PBE + U + spin-orbit coupling (SOC), were performed to obtain the magnetic anisotropy energy along with the spin and orbital magnetic moments.

B. Magnetic properties

Here we discuss the PBE + U + SOC results with $Nd_2Fe_{14}B$, using ML for H_c prediction. Hubbard U correction is necessary for highly correlated $3d$ and $4f$ elements [108–111] to accurately predict K_u. We performed test calculations for various values of U from 4–7 eV for Nd $4f$ orbitals. Table V shows the spin and orbital magnetic moments of Nd, Fe, and B at different crystallographic sites for different values of U_{eff}. The nonmagnetic B atom carries negligible magnetic moments. Nd exhibits an Nd^{3+} state with spin magnetic moment (μ_s) of approximately -3.3 and strongly quenched orbital moment (μ_l) of approximately 1.5 μ_B due to the crystalline electric field. The spin and orbital moments have opposite signs, consistent with Hund's rule for a less than half-filled $4f$ shell. The net magnetic moment is robust, and does not vary significantly with U.

Table VI lists K_u, M_s, T_C, and their comparison with experimental values. K_u is positively correlated with U. The experimental K_u is 4.5 MJ/m^3 [112] at 300 K, which corresponds to the computed value for $U \sim 4$ eV. T_C is computed with the static Green's function (GF) as implemented in ASA in the local density approximation (LDA) [113] for the exchange-correlation functional in the linearized muffin-tin orbital (LMTO) program [114,115]. The pair exchange interaction $J_{RR'}$ between magnetic R and R' ions is computed using the Lichtenstein formula [116], from which T_C is estimated. The calculated Weiss mean-field theory [117] value of 718.1 K is larger than the experimental value, which is expected in the mean-field approximation (MFA). According to a spin-wave theory by Tyablikov [118], the random-phase approximation (RPA) corrects the value, bringing it down to 539.1 K. The experimental value lies within the MFA and RPA limits.

Next, we discuss the site-resolved spin-orbit anisotropy energy, which is computed as $E_{\text{anis}} = E_{100} - E_{001}$[109], where E_{100} and E_{001} are PBE + U + SOC-computed atomic site energies for spin quantization along the [100] and [001] directions. Generally, $4f$ elements contribute to K_u, and $3d$ elements contribute to the magnetic moments in rare-earth-based magnets. The spin moments of the rare-earth ion are antiparallel to the spin moment of the $3d$ ion, which is also the case for neomagnets. The site contribution of the Nd element to crystalline anisotropy energy is given in Table VII. In our PBE + U + SOC calculations, we did not impose symmetry, which means that all the atoms are inequivalent under the P_1 crystal symmetry. All eight Nd atoms split into eight different sites. The individual on-site energies differ significantly for the atoms of

TABLE V. Spin and orbital magnetic moments (μ_s and μ_l) of individual atoms in different Wyckoff positions, and total magnetic spin and orbital magnetic moments (μ_{st} and μ_{lt}) per unit cell (in μ_B), in $Nd_2Fe_{14}B$ computed using the PBE + U + SOC method with various values of U for the Nd ($4f$) electronic states. There are two $16k$ and $8j$ sites, therefore, the pairs are given. The μ_l of the pair at $8j$ sites do not differ, and only one value is given to represent both atoms.

Atom →	Nd(4*f*)		Nd(4*g*)		Fe(16*k*)		Fe(8*j*)		Fe(4*e*)		Fe(4*c*)		B(4*g*)		Total	
U ↓	μ_s	μ_l	μ_s	μ_l	μ_s	μ_l	μ_s	μ_l	μ_s	μ_l	μ_s	μ_l	μ_s	μ_l	μ_{st}	μ_{lt}
4 eV	−3.26	1.52	−3.28	1.53	2.27, 2.36	0.043, 0.049	2.29, 2.71	0.044	2.03	0.045	2.48	0.054	−0.17	0.00	105.24	14.75
5 eV	−3.26	1.52	−3.28	1.53	2.27, 2.36	0.042, 0.048	2.29, 2.70	0.044	2.03	0.045	2.47	0.052	−0.17	0.00	105.25	14.75
7 eV	−3.27	1.52	−3.28	1.53	2.27, 2.36	0.042, 0.048	2.29, 2.71	0.042	2.03	0.044	2.48	0.049	−0.17	0.00	105.25	14.68

TABLE VI. Calculated K_u in MJ/m^3, M_s in μ_B/f.u. using PBE + U + SOC, T_c in Kelvin (K) using Green's function ASA (LDA), and comparison with available experiment.

U	K_u	M_s	M_s (Expt. [19])	T_C	T_C (Expt. [19])
4 eV	6.16	29.98	37.7[a], 32.5[b]	718.1[c], 539.1[d]	585
5 eV	8.56	30.00	...		...
7 eV	11.58	30.01	...		...

[a] At low temperature, (4 K).
[b] At high temperature (295 K).
[c] Mean-field approximation (MFA).
[d] Random-phase approximation (RPA).

the same crystallographic site. Interestingly, at least one Nd (Nd$_1$) at 4f has a negative contribution to crystalline anisotropy energy, as given in Table VII. Theoretically, it can be inferred that Nd has a tendency to be planar at the 4f site, differing from the 4g site, which is strictly uniaxial along the crystalline c direction. These results are consistent with experiment [119].

Table VIII shows the computed values of the magnetic moments and magnetic anisotropy in the Ce-substituted neomagnet at Nd-4f sites. The Ce-atom carries a small spin magnetic moment approximately $1\mu_B$ compared to the Nd approximately $3\mu_B$ moment. Moreover, the orbital moment does not entirely cancel the spin moment in Nd, unlike in Ce, where the net spin + orbital moment vanishes. Therefore, there is an increase in the net magnetic moment with Ce. On the other hand, magnetic anisotropy is reduced because the Ce-site contribution is much smaller than that of Nd. The calculated value of K_u slightly underestimates the experiment (see Table I), which is reasonable, given the choice of the U values used for the Ce and Nd 4f states. We used $U_{\text{eff}} = 2$ eV for Ce and 4 eV for Nd in the calculations.

C. ML coercivity prediction

Central to this paper is the hypothesis that macroscopic measures of H_c are not well predicted by theory, while the microscopic magnetic parameters M_s, K_u, and A_{ex} are. However, knowledge of the microscopic parameters is sufficient to produce realistic estimates of H_c by accumulating a database and modeling it with ML. Furthermore, once an ML prediction is made, information about the material grain structure may be reverse engineered with micromagnetic modeling. Although material fabrication variations have a significant impact on H_c, this section demonstrates the surprising effectiveness of the methodology as applied to $Nd_2Fe_{14}B$, with and without Ce doping.

The *ab initio*-calculated values were fed to the tuned XGB ML model to produce the output predictions. Additionally, micromagnetic simulation was used to determine a hysteresis loop. The results are depicted in Table IX. As can be seen in Fig. 11, the reduction trend of H_c with Ce is similar to that found experimentally [120]. Further, we computed the ML [trained with experiment (ML expt.) and scaled micromagnetic data (ML mumax^3) separately] and scaled micromagnetic simulated H_c for $SmCo_5$, YCo_5, $CeZrFe_{11}$, $CeZrFe_{11}N$, $CeTiFe_{11}$, and $CeTiFe_{11}N$ using DFT intrinsic parameters as given in Table IX. The ML expt. predicts inconsistent H_c due to the small data size training, as evident from model performance metrics in Table II. The ML mumax^3 trained on big datasets produces more sensible H_c than scaled-micromagnetics and ML expt. For $SmCo_5$, micromagnetic simulation yielded a factor of 3 larger H_c than the ML mumax^3 model and experiments. For YCo_5, the ML mumax3^3 model produced slightly lower H_c than the experiment, attributed to the DFT underestimate of K_1. Overall, the ML mumax^3 model consistently tends to correct the micromagnetically predicted H_c towards experiments for known materials (see Table I).

If the fabricated material is grown as a crystal with well-defined grains, it is possible to reverse engineer

TABLE VII. Site-resolved spin-orbit anisotropy energy (E_{anis}) in meV of the Nd contribution to magnetocrystalline anisotropy energy. In PBE + U + SOC calculations, the crystalline symmetry lowers to the P_1 point group implying that the atoms (including the Nd) split into eight sites. The negative value for Nd at the 4f site indicates it produces a planar contribution to the crystalline anisotropy energy, consistent with experiment [119].

Atom	Wyckoff position	E_{aniso}
Nd$_1$	4f	1.3780
Nd$_2$	4f	−1.1914
Nd$_3$	4f	0.5336
Nd$_4$	4f	6.2204
Nd$_5$	4g	0.4865
Nd$_6$	4g	3.8064
Nd$_7$	4g	6.2094
Nd$_8$	4g	3.0622

TABLE VIII. Total spin, orbital, and spin + orbital magnetic moments μ_s, μ_l, and $\mu_s + \mu_l$ in μ_B/cell, K_u in MJ/m^3, and M_s in MA/m of $Ce_2Fe_{14}B$ and $Nd_2Fe_{14}B$.

Properties	$Nd_2Fe_{14}B$	$Ce_2Fe_{14}B$
μ_s	105.24	120.73
μ_l	14.75	4.55
$\mu_s + \mu_l$	119.99	125.28
K_u	6.16	1.21
M_s	1.31	1.24

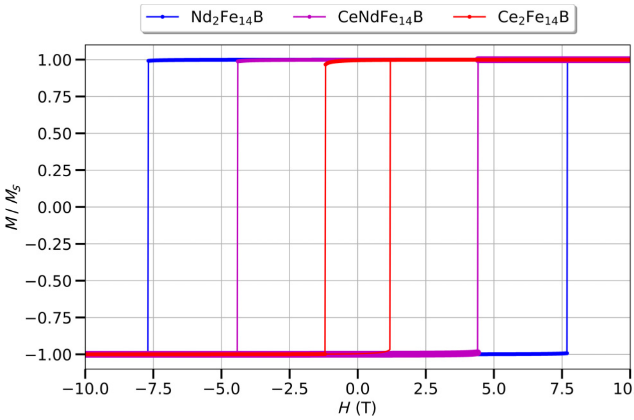

FIG. 11. Hysteresis curve for $Nd_{2-x}Ce_xFe_{14}B$ ($x = 0, 1.0, 2.0$) calculated from micromagnetic simulation. Ce leads to the reduction in the coercivity. M/M_s is the reduced magnetization.

TABLE IX. Comparison of ML predicted and scaled-micromagnetic (cH_c) H_c in T for materials with calculated DFT parameters. ML expt. and ML mumax^3 represent predictions made by training experimental and scaled-micromagnetic data.

Material	ML expt.	ML mumax^3	cH_c
$Nd_2Fe_{14}B$	3.92	2.39	2.35
$CeNdFe_{14}B$	0.88	1.27	1.29
$Ce_2Fe_{14}B$	0.39	0.40	0.36
$SmCo_5$	8.87	5.88	18.12
YCo_5	1.45	1.51	1.60
$CeZrFe_{11}$	6.25	4.93	5.99
$CeZrFe_{11}N$	1.51	2.15	2.59
$CeTiFe_{11}$	1.50	2.09	2.70
$CeTiFe_{11}N$	1.51	1.92	2.45

the structure. The dependence of H_c on micromagnetic parameters, viz., grain sizes and intergrain coupling is visualized in Fig. 12 in the 128 × 128 × 128 nm^3 magnetic cell. Here, the grain coupling refers to a reduction factor to the stiffness exchange coupling A_{ex}. We note that we did not find much difference in the results with the use of 64 × 64 × 64 and 128 × 128 × 128 nm^3 simulation cells. Although nonlinear, we find a similar trend of H_c with intergrain exchange coupling and grain sizes. For a fixed value of grain size, qualitatively, H_c decreases with intergrain exchange coupling, while it is the opposite with grain size. That intergrain exchange coupling may not be uniform in actual material due to the void or imperfection between the grains, which affects the perfect spin alignment resulting in M_s. A larger intergrain exchange coupling further reduces K_1 and H_c. With an increase in grain size, H_c experiences a decrease, similar to that reported in the Dy-substituted neomagnet [121].

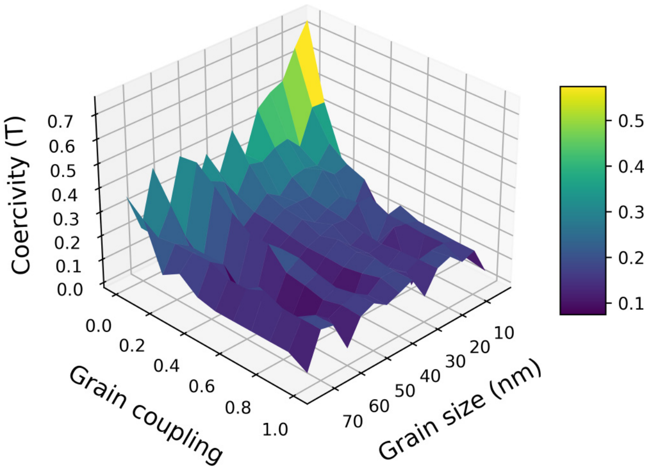

FIG. 12. Coercivities for different intergrain couplings for $Nd_2Fe_{14}B$, measured as a function of the ratio of intergrain exchange stiffness to intragrain exchange stiffness and different grain sizes. As the material is complex, a cuboid of 128 × 128 × 128 nm^3 was generated for each grain size, resulting in some random undulations according to grain initialization. The plot displays a decreasing coercivity with increasing grain size as observed in experiment [120].

Various combinations of grain size and intergrain exchange coupling reproduce the actual coercivity. For instance, with grain size approximately 30 nm, and a 0.58 ratio for intergrain to intragrain A_{ex} reproduces the realistic H_c of 0.40 T, as demonstrated in Fig. 13. Strictly speaking, a larger intergrain coupling tends to reduce the H_c, regardless of grain size. This suggests that we can explore the other magnetic parameters A_{ex} and grain size by using ML-predicted results employing micromagnetic simulations, which demonstrates the fundamental usefulness of ML, not just as a black box but also as a preprocessing input to a micromagnetic model to reverse engineer the micromagnetic structure.

V. CONCLUSION

Experimental dataset input and ML modeling coupled with DFT predicts H_c with far greater accuracy and speed

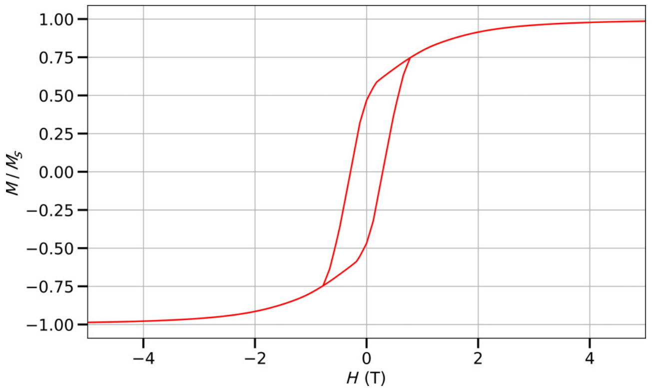

FIG. 13. Hysteresis curve for $Ce_2Fe_{14}B$ calculated naively with micromagnetic simulation with grain size set to 30 nm and intergrain stiffness to intragrain stiffness set at 0.58 to recreate the ML H_c prediction.

TABLE X. Hyperparameters used for XGB model training of experimental magnetic materials.

n_estimators = 500
min_weight_fraction_leaf = 0
max_depth = 5
learning_rate = 0.006

than was previously possible using micromagnetic modeling. This technique provides a robust computational foundation for predicting alternative permanent magnet materials and optimizing their properties. Using micromagnetic simulation, we first studied magnetization as a function of the applied magnetic field for real and hypothetical magnetic materials, mainly focusing on 1:5 and 2:14:1 rare-earth-based permanent magnets such as $Nd_2Fe_{14}B$. Calculations of H_c based on the hysteresis loop overestimate by a factor of approximately 5; the Brown paradox. The paradox is side stepped by the judicious use of ML, obtaining a more accurate prediction of the target variable by learning its dependence on the input features. We find that H_c is directly proportional to K_u, inversely proportional to M_s, and weakly correlated with A_{ex}.

We apply the ML modeling to $Nd_2Fe_{14}B$ by first computing its independent variables with DFT calculations. These calculations show that the Nd 4*g* sites mainly contribute to the uniaxial magnetocrystalline anisotropy. They also yield a value for the T_C, which agrees with the experiment. The DFT predictions suggest the possibility of tuning rare-earth magnetic properties by substituting noncritical elements at specific sites. For instance, Ce doping at 4*f* sites shows only a slight reduction in H_c, consistent with the ML prediction. Finally, we engineer the grain-boundary size and interexchange coupling with the aid of ML-predicted H_c, which indicates that the reduction in intergrain exchange coupling reduces H_c. On the other hand, reducing the grain size increases H_c qualitatively.

ACKNOWLEDGMENTS

This work is supported by the Critical Materials Innovation Hub, an Energy Innovation Hub funded by the US Department of Energy, Office of Energy Efficiency and Renewable Energy, Advanced Materials and Manufacturing Technologies Office. The Ames National Laboratory is operated for the U.S. Department of Energy by Iowa State University of Science and Technology under Contract No. DE-AC02-07CH11358. G.N.N. acknowledges support from the U.S. Department of Energy, Office of Science, Office of Workforce Development for Teachers and Scientists, Office of Science Graduate Student Research (SCGSR) program. The SCGSR program is administered by the Oak Ridge Institute for Science and Education for the DOE under Contract No. DE-SC0014664.

TABLE XI. Fine-tuned hyperparameters for different ML models used in the training of micromagnetic simulated data.

Model	Hyperparameters
Tuned RF	n_estimators = 1200, max_depth = 5, random_state = 1, min_samples_leaf = 3, bootstrap = True, max_features = “auto”
Tuned XGB	n_estimators = 1200, max_depth = 5, min_weight_fraction_leaf = 0, learning_rate = 0.007
Tuned XGB	n_estimators = 1200, max_depth = 5, min_child_weight = 0, learning_rate = 0.007, random_state = 42

TABLE XII. DFT computed intrinsic magnetic parameters for 1 : 12 compositions taken from our previous work [111] except for 1 : 5 type materials as referred to in the table. A_{ex} is kept fixed for all materials.

Material	M_s (A/m)	A_{ex} (pJ/m)	K_u (MJ/m^3)
$SmCo_5$ [122]	1 069 768.213	7	40.27
YCo_5 [123]	770 449.2281	7	2.65
$CeZrFe_{11}$	597 220.2602	7	7.36
$CeZrFe_{11}N$	632 804.6376	7	3.42
$CeTiFe_{11}$	587 261.7154	7	3.29
$CeTiFe_{11}N$	625 792.1247	7	3.20

APPENDIX A: ML MODEL AND HYPERPARAMETER TUNING

In this Appendix we provide information about the hyperparameters used in the fine tuning of the ML models. With the experimental data, we used the hyperparameters given in Table X for tuned XGB model training.

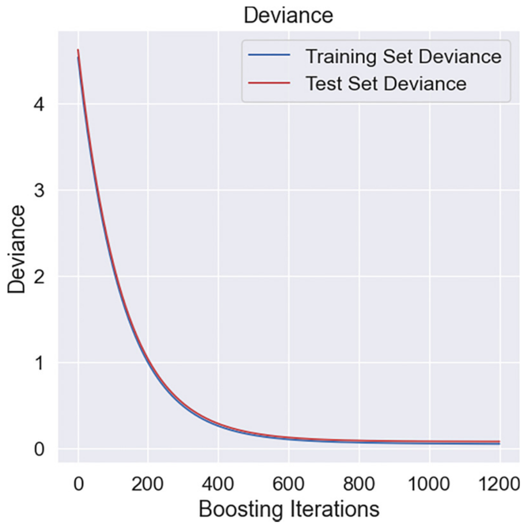

FIG. 14. Deviance as a function of boosting iterations for the micromagnetic simulated dataset with XGB model. Deviance is MSE between the actual and predicted dataset computed in each iteration. Both the training and test dataset converge well after 600 boosting iterations.

In mumax^3 data training we use the hyperparameters given in Table XI.

The hyperparameter used in the fine-tuned GBR model training is shown in Fig. 14. The deviance (MSE) converges well in both the test and training datasets after 600 boosting iterations, confirming a very good model performance.

APPENDIX B: DFT PARAMETERS FOR 1 : 5 AND 1 : 12 INTERMETALLICS

Table XII provides the DFT computed parameters for 1 : 5 and 1 : 12 intermetallic compounds.

1. Experimental database

In Table XIII, we provide the experimental database obtained from the literature [19,26–80]. For some materials, independent variables are different in different experiments leading to the distinct values for H_c. For clarity, they are labeled with $-A/B/C$ at the end of compound names in the table. In ML training we utilized 211 materials for which we are confident at the H_c experimentally measured or interpolated from the existing database.

TABLE XIII. Magnetic database for 300 experimental materials. The numerical values at the end of compound column refer to the x or y variables for the nonstoichiometric compositions. Materials without asterisks have H_c values obtained directly from the literature. An asterisk indicates the need to calculate H_c using the methods described in the paper. Series of materials (substitution or different ratios of material combinations in the case of an element of the form A_xB_{1-x}) have their values linearly interpolated in the case that all values are not reported.

Material	M_s (MA/m)	A_{ex} (pJ/m)	K_u (MJ/m^3)	H_c (T)
$La_2Fe_{14}B$	1.098	7.410	1.400	0.500
$Ce_2Fe_{14}B$	0.931	6.000	1.700	0.540
$Pr_2Fe_{14}B$	1.241	7.940	4.660	1.540
$Nd_2Fe_{14}B$	1.273	8.230	4.650	1.240
$Gd_2Fe_{14}B$	0.708	9.330	0.850	0.234
$Tb_2Fe_{14}B$	0.557	8.780	6.130	2.930
$Dy_2Fe_{14}B$	0.565	9.420	4.240	1.700
$Ho_2Fe_{14}B$	0.644	8.140	2.420	0.750
$Lu_2Fe_{14}B$	0.931	7.660	1.210	0.294
$Y_2Fe_{14}B$	1.122	8.010	1.460	0.187
$Th_2Fe_{14}B$	1.122	6.770	1.460	0.170
$La_2Co_{14}B$	0.792	15.000	1.189	0.345
$Pr_2Co_{14}B$	1.040	15.100	5.201	2.500
$Nd_2Co_{14}B$	1.076	15.100	2.422	3.694
$Gd_2Co_{14}B$	0.229	15.200	1.034	0.300
$Y_2Co_{14}B$	0.847	15.201	1.187	0.344
Nd-La-Ce-Fe-B	0.746	6.000	2.250	0.652
La-Ce-Y-Fe-B	0.525	6.000	1.500	0.415
$NdPrFe_{14}B$	1.273	7.700	4.200	0.800
$(Nd_{0.91}Ce_{0.089})_2Fe_{14}B$	1.242	8.083	4.500	1.100
$(Nd_{0.78}Ce_{0.22})_2Fe_{14}B$	1.268	7.864	4.600	1.030
$(Nd_{0.62}Ce_{0.38})_2Fe_{14}B$	1.200	7.673	3.100	0.900
$Nd_2Fe_{14}B$-alloy	1.129	10.000	4.900	1.420
48H,Nd-Fe-B	1.107	10.000	6.039	1.750
$Tb_{75}Cu_{25}$	1.081	10.000	10.007	2.900
$Tb_{65}Ce_{10}Cu_{25}$	1.074	10.000	9.662	2.800
$Tb_{55}Ce_{20}Cu_{25}$	1.093	10.000	9.662	2.800
$Tb_{45}Ce_{30}Cu_{25}$	1.097	10.000	9.179	2.660
$Tb_{30}Ce_{45}Cu_{25}$	1.103	10.000	8.868	2.570
$Nd_{12}Fe_{82}B_6$	1.461	7.651	4.500	1.094
$Nd_{11}Ce_1Fe_{82}B_6$	1.354	7.459	4.125	1.040
$Nd_{10}Ce_2Fe_{82}B_6$	1.325	7.268	3.750	0.961
$Nd_8Ce_4Fe_{82}B_6$	1.276	6.886	3.000	0.844
$Nd_6Ce_6Fe_{82}B_6$	1.208	6.503	2.250	0.768
$Nd_4Ce_8Fe_{82}B_6$	1.111	6.120	1.950	0.684
$Nd_2Ce_{10}Fe_{82}B_6$	1.049	5.738	1.560	0.518
$Nd_1Ce_{11}Fe_{82}B_6$	0.905	5.547	1.430	0.405
$Ce_{12}Fe_{82}B_6$	0.751	5.355	1.300	0.315
MnAl(300 K)	0.801	3.484	0.150	0.024
CoPt(300 K)	0.603	6.770	6.062	0.951
FePt(300 K)	1.145	6.660	1.140	0.179
FePd(4 k)	1.192	6.507	1.841	0.289
Fe_3Sn	1.180	7.772	1.800	1.483
$Fe_{2.5}Mn_{0.5}Sn_{0.95}Sb_{0.05}$	1.020	6.893	1.150	0.947
$Fe_{1.5}Mn_{1.5}Sn_{0.90}Sb_{0.10}$	0.680	4.331	0.010	0.008

TABLE XIII. Continued.

$Fe_{1.5}Mn_{1.5}Sn_{0.85}Sb_{0.15}$	0.650	4.285	0.010	0.008
Fe_5SN_3 (1100 K)	0.700	6.398	0.005	0.004
Fe_5SN_3 (1155 K)	0.750	7.599	0.005	0.004
Fe_5SN_3 Crystal (1100 K)	0.700	7.418	0.350	0.288
FeNi(300 K)	1.273	3.300	1.323	0.140
Fe_5Ge	1.432	14.700	0.230	0.002
L10 FeNi(Si substrate)*	1.193	10.000	0.380	0.029
$Fe_3Sn_{0.75}Sb_{0.25}$*	1.209	10.000	0.330	0.051
$CoFe_6Ta$*	1.448	14.900	1.000	0.099
L10FeNi(bulk)*	1.098	10.000	1.100	0.140
MnAl*	0.636	7.600	0.700	0.186
$Nd_{0.2}Zr_{0.8}Fe_{10}Si_2$*	0.891	10.000	1.160	0.210
$Sm_{0.7}Zr_{0.3}Fe_{10}Si_2$*	0.859	10.000	3.500	0.199
Alnico5*	1.120	6.600	0.680	0.071
CoPt*	0.800	14.000	4.900	1.400
FePt*	1.140	12.000	6.600	0.800
$SmCo_5$-A*	0.860	12.000	17.200	7.500
Pr_2Co_{17}*	0.847	4.244	5.090	0.038
$Pr_{1.64}Sm_{0.36}Fe_{17}$*	0.749	4.455	2.490	0.019
Sm_2Co_{17}	0.970	14.424	3.300	1.250
$Nd_2Fe_{14}B$	1.280	8.965	4.900	2.000
$Sm_2Fe_{17}N_3$	1.230	10.966	8.600	2.300
YCo_5	0.779	7.110	5.500	3.900
$LaCo_5$	0.712	6.470	6.300	5.250
$CeCo_5$	0.597	5.130	6.400	5.700
$PrCo_5$	0.939	6.960	8.100	5.325
$NdCo_5$	0.933	7.090	0.240	0.150
$MMCo_5$	0.715	4.720	6.400	5.620
$MM_{0.8}Sm_{0.2}Co_5$	0.779	5.757	7.800	6.855
$Sm_{0.6}Gd_{0.4}Co_5$	0.580	5.683	7.700	6.768
$Sm_2(Co_{0.7}Pe_{0.3})17$	1.154	2.214	3.000	2.637
$Sm_2(Co_{0.8}Pe_{0.1})17$	1.042	3.174	4.300	3.779
$Sm(Co_{0.87}Cu_{0.13})7.8$	0.867	2.436	3.300	2.900
Fe_2P*	0.668	12.170	0.770	0.027
$(Fe_{0.91}Co_{0.09})2P_{0.89}Si_{0.11}$*	0.716	13.332	0.860	0.014
$(Fe_{0.91}Co_{0.09})2P_{0.86}Si_{0.14}$*	0.732	13.913	0.890	0.008
$(Fe_{0.91}Co_{0.09})2P_{0.81}Si_{0.19}$*	0.763	14.835	1.090	0.004
$(Fe_{0.92}Co_{0.08})2P_{0.78}Si_{0.22}$*	0.803	16.419	0.930	0.002
$(Fe_{0.91}Co_{0.09})2P_{0.74}Si_{0.26}$*	0.380	11.000	0.330	0.470
Co	0.371	5.723	0.274	0.392
Fe	0.303	5.868	0.287	0.432
$Fe_{70}Co_{30}$	0.362	5.478	0.334	0.583
$Fe_{60}Co_{20}B_{20}$	0.420	6.100	0.310	0.503
$Co_{93}Gd_7$	0.415	5.999	0.293	0.450
$Co_{80}Gd_{20}$	0.465	5.716	0.302	0.476
$CoFe_2O_4$	0.434	5.706	0.298	0.465
$CoEu_{0.03}Fe_{1.97}O_4$	0.451	5.489	0.280	0.409
$CoEu_{0.06}Fe_{1.94}O_4$	0.391	6.238	0.281	0.413
$CoEu_{0.09}Fe_{1.91}O_4$	0.331	6.099	0.265	0.366
$CoEu_{0.12}Fe_{1.88}O_4$	0.350	5.976	0.254	0.338
$BaFe_{12}O_{19}$	0.326	5.677	0.215	0.241
$SrFe_{12}O19$	0.267	5.894	0.253	0.335
$Sr_{0.7}La_{0.3}Fe_{12}O_{19}$	0.272	5.898	0.251	0.329
$SrLaFe_xCo_xAl_xO0.2$	0.283	5.900	0.255	0.339
$SrLaFe_xCo_xAl_xO0.4$	0.278	5.839	0.306	0.488
$SrLaFe_xCo_xAl_xO0.6$	0.289	5.284	0.303	0.481
$SrLaFe_xCo_xAl_xO0.8$	0.300	5.288	0.268	0.376
$Sr_{0.7}Pr_{0.3}Fe_{12}O_{19}$	0.192	5.279	0.293	0.449
$SrPrFe_xCo_xAl_xO0.2$	0.293	5.284	0.257	0.345
$SrPrFe_xCo_xAl_xO0.4$	0.318	5.291	0.210	0.230
$SrPrFe_xCo_xAl_xO0.6$	0.265	4.906	0.288	0.434
$SrPrFe_xCo_xAl_xO_{0.8}$	0.273	5.426	0.287	0.431
$BaFe_{12}O_{19}$-B	0.323	5.424	0.285	0.426
Al900	0.400	5.693	0.218	0.248
Al950	0.398	5.684	0.228	0.272
Al1000	0.387	5.653	0.231	0.280
Bi900	0.364	5.646	0.221	0.256
Bi950*	0.201	6.000	0.340	0.322
Bi1000*	0.144	5.969	0.267	0.253
Cr900*	0.111	5.945	0.214	0.203
Cr950*	0.070	5.911	0.139	0.132
Cr1000*	0.050	5.895	0.838	0.793
Mn900*	0.036	5.868	0.086	0.081
Mn950*	0.232	5.215	0.340	0.329
Mn1000*	0.201	4.268	0.377	0.404

TABLE XIII. Continued.

$Sr_{1-x}Nd_xFe_{12}O_{19}$0.0∗	0.190	3.796	0.421	0.503
$Sr_{1-x}Nd_xFe_{12}O_{19}$0.05∗	0.164	2.769	0.459	0.600
$Sr_{1-x}Nd_xFe_{12}O_{19}$0.1∗	0.159	2.216	0.508	0.734
$Sr_{1-x}Nd_xFe_{12}O_{19}$0.15∗	0.292	0.413	0.462	0.608
$BaFe_{12}O_{19}$-C	0.308	0.338	0.416	0.492
$BaFe_{12-2x}Al_xCr_xO_{19}$0	0.332	0.411	0.284	0.230
$BaFe_{12-2x}Al_xCr_xO_{19}$0.2	0.334	0.276	0.274	0.213
$BaFe_{12-2x}Al_xCr_xO_{19}$0.4	0.328	0.304	0.216	0.133
$BaFe_{12-2x}Al_xCr_xO_{19}$0.6	0.294	0.295	0.197	0.110
$BaFe_{12-2x}Al_xCr_xO_{19}$0.8	0.369	5.700	0.497	0.704
$BaFe_{12-2x}Al_xCr_xO_{19}$1	0.371	5.700	0.507	0.731
$SrCr_xFe_{12-x}O_{19}$0	0.370	5.710	0.516	0.758
$SrCr_xFe_{12-x}O_{19}$0.3	0.375	5.710	0.522	0.775
$SrCr_xFe_{12-x}O_{19}$0.5	0.373	5.710	0.526	0.788
$SrCr_xFe_{12-x}O_{19}$0.7	0.366	5.710	0.512	0.747
$SrCr_xFe_{12-x}O_{19}$0.9	0.358	5.710	0.510	0.742
$SrCo_xZr_xFe_{12-2x}O_{19}$0	0.342	5.710	0.509	0.739
$SrCo_xZr_xFe_{12-2x}O_{19}$0.2	0.306	5.710	0.502	0.718
$SrCo_xZr_xFe_{12-2x}O_{19}$0.4	0.358	6.000	0.183	0.096
$SrCo_xZr_xFe_{12-2x}O_{19}$0.6	0.365	5.700	0.121	0.042
$SrCo_xZr_xFe_{12-2x}O_{19}$0.8	0.358	5.400	0.028	0.040
$SrCo_xZr_xFe_{12-2x}O_{19}$1	0.340	5.100	0.067	0.097
$Sr_{0.75-x}La_{0.25}Ca_xFeCoO$0	0.323	4.800	0.066	0.097
$Sr_{0.75-x}La_{0.25}Ca_xFeCoO$0.05	0.309	4.500	0.087	0.129
$Sr_{0.75-x}La_{0.25}Ca_xFeCoO$0.1	0.369	5.700	0.410	0.273
$Sr_{0.75-x}La_{0.25}Ca_xFeCoO$0.15	0.369	5.130	0.424	0.298
$Sr_{0.75-x}La_{0.25}Ca_xFeCoO$0.2	0.363	4.850	0.412	0.328
$Sr_{0.75-x}La_{0.25}Ca_xFeCoO$0.25	0.356	4.560	0.408	0.352
$Sr_{0.75-x}La_{0.25}Ca_xFeCoO$0.3	0.348	4.280	0.403	0.375
$Sr_{0.75-x}La_{0.25}Ca_xFeCoO$0.4	0.347	3.990	0.405	0.405
$Sr_{0.75-x}La_{0.25}Ca_xFeCoO$0.6	0.354	5.700	0.382	0.247
$SrCaLa_x$0	0.357	5.130	0.422	0.342
$SrCaLa_x$0.1	0.361	4.850	0.415	0.318
$SrCaLa_x$0.2	0.351	4.560	0.414	0.336
$SrCaLa_x$0.3	0.349	4.280	0.411	0.367
$SrCaLa_x$0.4	0.350	3.990	0.409	0.415
$SrCaLa_x$0.5	0.343	5.884	0.297	0.652
$Sr_{1-x}La_xFe_{12-x}Co_xO_{19}$-del-sin0	0.333	5.822	0.291	0.726
$Sr_{1-x}La_xFe_{12-x}Co_xO_{19}$-del-sin0.1	0.330	5.753	0.292	0.770
$Sr_{1-x}La_xFe_{12-x}Co_xO_{19}$-del-sin0.15	0.325	5.696	0.292	0.780
$Sr_{1-x}La_xFe_{12-x}Co_xO_{19}$-del-sin0.2	0.320	5.626	0.289	0.804
$Sr_{1-x}La_xFe_{12-x}Co_xO_{19}$-del-sin0.25	0.302	5.556	0.288	0.755
$Sr_{1-x}La_xFe_{12-x}Co_xO_{19}$-del-sin0.3	0.274	5.487	0.289	0.662
$Sr_{1-x}La_xFe_{12-x}Co_xO_{19}$-del-ane0	0.308	6.000	0.313	0.203
$Sr_{1-x}La_xFe_{12-x}Co_xO_{19}$-del-ane0.1	0.293	0.908	0.279	0.190
$Sr_{1-x}La_xFe_{12-x}Co_xO_{19}$-del-ane0.15	0.279	23.752	0.151	0.108
$Sr_{1-x}La_xFe_{12-x}Co_xO_{19}$-del-ane0.2	0.280	6.409	0.108	0.077
$Sr_{1-x}La_xFe_{12-x}Co_xO_{19}$-del-ane0.25	0.287	6.890	0.122	0.085
$Sr_{1-x}La_xFe_{12-x}Co_xO_{19}$-del-ane0.3	0.295	7.179	0.138	0.093
$Sr_{1.05-x}La_xFe_{12-x}Co_xO_{19}$0	0.274	5.610	0.295	0.158
$Sr_{1.05-x}La_xFe_{12-x}Co_xO_{19}$0.1	0.871	4.418	0.044	0.020
$Sr_{1.05-x}La_xFe_{12-x}Co_xO_{19}$0.2	0.865	4.565	0.667	0.300
$Sr_{1.05-x}La_xFe_{12-x}Co_xO_{19}$0.3	0.847	4.771	2.667	1.200
$Sr_{1.05-x}La_xFe_{12-x}Co_xO_{19}$0.4	0.830	4.844	4.889	2.200
$Sr_{1.05-x}La_xFe_{12-x}Co_xO_{19}$0.5	0.822	4.852	4.889	2.200
$Sr_{1.05-x}La_xFe_{12-x}Co_xO_{19}$0.6	0.810	4.874	3.556	1.600
$Sr_{1-x}Ce_xFe_{12}O_{19}$0	0.860	4.823	4.000	1.800
$Sr_{1-x}Ce_xFe_{12}O_{19}$0.05	1.034	13.800	2.500	1.208
$Sr_{1-x}Ce_xFe_{12}O_{19}$0.1	1.098	13.400	1.600	0.728
$Sr_{1-x}Ce_xFe_{12}O_{19}$0.15	0.708	8.300	16.500	11.649
$Sr_{1-x}Ce_xFe_{12}O_{19}$0.2	0.652	8.000	15.100	11.570
$Sr_{1-x}Ce_xFe_{12}O_{19}$0.25	0.604	7.700	13.500	11.161
$Sr_{1-x}Ce_xFe_{12}O_{19}$0.3	0.557	7.400	12.000	10.771
$Sm_2Fe_{15}Ga_2$∗	0.517	7.100	10.400	10.053
$Sm_2Fe_{14.5}Cu_{0.5}Ga_2$∗	0.431	9.910	3.991	1.700
$Sm_2Fe_{14.5}Cu_{0.5}Ga_2C_{0.5}$∗	0.351	9.860	4.460	1.900
$Sm_2Fe_{14.5}Cu_{0.5}Ga_2C_{1.0}$∗	0.344	9.890	5.634	2.400
$Sm_2Fe_{14.5}Cu_{0.5}Ga_2C_{1.5}$∗	0.394	9.880	9.343	3.980
$Sm_2Fe_{14.5}Cu_{0.5}Ga_2C_{2.0}$∗	0.332	10.000	10.000	4.260
$Sm_2Fe_{15}Ga_2C_{1.0}$	1.330	20.000	2.000	0.700
$Sm_2(Co_{0.90}Fe_{0.1})17$	0.779	12.300	9.240	2.333
$Sm_2(Co_{0.80}Fe_{0.2})17$	0.619	7.977	2.000	0.166
$Sm(Co_{0.95}Cu_{0.05})5$	0.534	7.262	1.800	0.515
$Sm(Co_{0.90}Cu_{0.1})5$	0.450	6.033	1.600	0.865
$Sm(Co_{0.85}Cu_{0.15})5$	0.362	5.493	1.300	1.213

TABLE XIII. Continued.

Sm(Co$_{0.80}$Cu$_{0.25}$)5	0.312	4.846	1.200	1.903
Sm(Co$_{0.75}$Cu$_{0.25}$)5	0.281	3.925	1.000	2.692
Sm(Co$_{0.90}$Cu$_{0.1}$)4.8, 5	0.239	2.994	0.800	1.221
Sm(Co$_{0.90}$Cu$_{0.1}$)4.8, 15	0.197	1.035	0.700	0.906
Sm(Co$_{0.90}$Cu$_{0.1}$)4.8, 30	0.641	4.176	0.900	0.046
Sm(Co$_{0.90}$Cu$_{0.1}$)4.8, 40	0.645	4.349	0.747	0.047
Sm(Co$_{0.90}$Cu$_{0.1}$)4.8, 50	0.703	4.537	0.593	0.046
SmCoCuTi$*$	0.708	4.689	0.440	0.044
Sm(Co$_{\mathrm{bal}}$Fe$_{0.1}$Cu$_{0.1}$Zr$_{0.033}$)6.93*	0.760	4.794	0.286	0.046
SmCo$_{4.5}$Cu$_{0.5}*$	0.971	6.284	1.200	0.047
SmCo$_4$Cu$*$	0.941	6.043	1.445	0.062
SmCo$_{3.5}$Cu$_{1.5}*$	0.939	6.100	1.689	0.070
SmCo$_3$Cu$_2*$	0.927	6.092	1.934	0.076
SmCo$_{2.5}$Cu$_{2.5}*$	0.922	6.148	2.178	0.091
SmCo$_2$Cu$_3*$	0.909	6.171	2.912	0.100
SmCoCu$_4*$	0.324	3.942	1.040	0.057
$0xy1$, Ce$_{1-x}$Nd$_x$Fe$_{12-y}$Mo$_y*$	0.438	3.973	0.060	0.050
$0.2xy1*$	0.536	4.091	0.061	0.050
$0.4xy1*$	0.585	4.256	0.064	0.049
$0.6xy1*$	0.650	4.356	0.062	0.047
$0.8xy1*$	0.681	4.490	0.070	0.041
$1xy1*$	0.767	5.743	0.063	0.038
$0xy1N*$	0.767	5.847	0.092	0.103
$0.2xy1N*$	0.748	5.975	0.118	0.152
$0.4xy1N*$	0.724	5.944	0.132	0.198
$0.6xy1N*$	0.699	5.962	0.142	0.248
$0.8xy1N*$	0.681	5.934	0.168	0.307
$1xy1N*$	0.173	3.454	0.182	0.050
$0xy15*$	0.187	3.592	0.037	0.040
$0.2xy15*$	0.269	3.763	0.044	0.040
$0.4xy15*$	0.301	3.832	0.054	0.044
$0.6xy15*$	0.383	3.994	0.057	0.038
$0.8xy15*$	0.480	4.211	0.061	0.037
$1xy15*$	0.613	4.928	0.056	0.034
$0xy15N*$	0.552	5.066	0.058	0.088
$0.2xy15N*$	0.575	5.214	0.157	0.170
$0.4xy15N*$	0.541	5.177	0.228	0.217
$0.6xy15N*$	0.534	5.267	0.287	0.290
$0.8xy15N*$	0.559	5.393	0.347	0.334
$1xy15N*$	0.161	6.600	0.419	0.135
$0xy2*$	1.020	5.900	0.017	0.151
$0.2xy2*$	0.251	6.130	0.015	0.162
$0.4xy2*$	0.426	6.310	0.022	0.170
$0.6xy2*$	0.505	6.320	0.027	0.178
$0.8xy2*$	0.227	3.630	0.029	0.322
$1xy2*$	0.609	12.000	0.035	0.178
$0xy2N*$	0.411	5.040	0.041	0.232
$0.2xy2N*$	0.401	4.950	0.097	0.310
$0.4xy2N*$	0.314	9.200	0.196	0.222
$0.6xy2N*$	1.122	9.370	0.235	1.499
$0.8xy2N*$	1.073	9.130	0.310	1.638
$1xy2N*$	0.999	8.790	0.374	1.863
Sm-Alnico-0.1	0.924	8.540	4.143	1.972
Sm-Alnico-10.7	0.826	8.300	3.789	2.018
Sm-Alnico-12	1.125	9.490	4.293	1.678
Sm-Alnico-13.3	1.087	9.330	4.653	1.882
Sm-Alnico-13.7	1.014	9.050	4.577	1.985
Sm-Alnico-16	0.930	8.720	4.448	2.102
Sm-Alnico-17	0.840	8.410	4.299	2.252
Sm-Alnico-17.6	1.144	9.620	4.675	1.798
Sm-Alnico-18.4	1.110	9.490	4.985	1.975
Sm-Alnico-19	1.048	9.340	4.898	2.056
Sm$_2$Co$_{16}$V0.2	0.961	9.130	4.883	2.235
Sm$_2$Co$_{16}$V0.4	0.865	8.950	4.871	2.477
Sm$_2$Co$_{16}$V0.6	1.121	9.630	3.981	1.562
Sm$_2$Co$_{16}$V0.8	1.069	9.590	3.789	1.559
Sm$_2$Co$_{16}$V1	0.983	9.480	3.521	1.575
Sm$_2$Co$_{16}$Ti$_{0.2}$	0.887	9.360	3.500	1.735
Sm$_2$Co$_{16}$Ti$_{0.3}$	0.887	9.360	3.500	1.735
Sm$_2$Co$_{16}$Ti$_{0.4}$	0.887	9.360	3.500	1.735
Sm$_2$Co$_{16}$Ti$_{0.5}$	0.887	9.360	3.500	1.735
Sm$_2$Co$_{16}$Ti$_{0.6}$	0.887	9.360	3.500	1.735
Sm$_2$Co$_{16}$Ti$_{0.7}$	0.887	9.360	3.500	1.735
Sm$_2$Co$_{16}$Ti$_{0.8}$	0.887	9.360	3.500	1.735
Sm$_2$Co$_{16}$Ti$_{0.9}$	0.887	9.360	3.500	1.735

TABLE XIII. Continued.

$Sm_2Co_{16}Ti_{0.10}$	0.887	9.360	3.500	1.735
$Sm_2Co_{16}Ti_{0.11}$	0.887	9.360	3.500	1.735
$Sm_2Co_{16}Ti_{0.12}$	0.887	9.360	3.500	1.735
$Sm_2Co_{16}Ti_{0.13}$	0.887	9.360	3.500	1.735
$Sm_2Co_{16}Ti_{0.14}$	0.887	9.360	3.500	1.735
$Sm_2Co_{16}Hf_{0.8}$*	0.950	8.640	4.219	0.670
$Sm_2Co_{16}Hf_{1.0}$*	0.885	8.490	4.253	0.911
Ce_2Co_{17}*	0.698	8.060	4.461	1.298
$Ce_2Co_{16}Cu_1$*	0.972	8.780	4.800	0.468
Ce_2Co_{16}V0.2*	0.918	8.700	5.973	0.582
Ce_2Co_{16}V0.4*	0.828	8.560	6.058	0.735
Ce_2Co_{16}V0.6*	0.614	8.320	6.812	1.043
Ce_2Co_{16}V1.0*	0.949	7.940	1.100	0.526
$Ce_2Co_{16}Ti_{0.2}$	0.899	7.030	1.471	0.703
$Ce_2Co_{16}Ti_{0.3}$	0.827	5.890	1.234	0.789
$Ce_2Co_{16}Ti_{0.6}$	0.755	4.470	1.020	0.731
$Ce_2Co_{16}Ti_{1.0}$	0.928	7.550	0.983	0.654
$Ce_2Co_{16}Zr_{0.2}$	0.886	5.930	1.137	0.676
$Ce_2Co_{16}Zr_{0.4}$	0.737	4.660	0.828	0.509
$Ce_2Co_{16}Zr_{0.6}$	0.513	3.140	1.200	0.427
$Ce_2Co_{16}Zr_{1.0}$	0.993	8.840	1.183	0.420
$Ce_2Co_{16}Hf_{0.2}$	1.018	8.740	1.377	0.482
$Ce_2Co_{16}Hf_{0.4}$	1.037	8.600	1.123	0.452
$Ce_2Co_{16}Hf_{0.6}$	1.059	8.440	1.169	0.440
$Ce_2Co_{16}Hf_{1.0}$	1.081	8.190	1.116	0.409
$Ce_2Co_{16}Cr_{0.2}$	1.101	7.920	1.100	0.375
$Ce_2Co_{16}Cr_{0.5}$	1.118	7.330	1.068	0.334
$Ce_2Co_{16}Cr_{1.5}$	1.138	6.660	1.128	0.314
$Ce_2Co_{16}Cr_{2.0}$	1.138	6.660	1.128	0.314

[1] J. F. Trevor Hastie and Robert Tibshirani, *The Elements of Statistical Learning*, 2nd ed., Springer Series in Statistics No. 2 (Springer New York, NY), p. XXII, 745.

[2] M. J. Crowder, A. C. Kimber, R. L. Smith, and T. J. Sweeting, *Statistical analysis of reliability data* (Chapman & Hall, London, 1991), 1st ed.

[3] W. F. Brown, Virtues and weaknesses of the domain concept, Rev. Mod. Phys. **17**, 15 (1945).

[4] A. Aharoni, Theoretical search for domain nucleation, Rev. Mod. Phys. **34**, 227 (1962).

[5] U. Hartmann, Origin of Brown's coercive paradox in perfect ferromagnetic crystals, Phys. Rev. B **36**, 2331 (1987).

[6] T. Xie and J. C. Grossman, Crystal graph convolutional neural networks for an accurate and interpretable prediction of material properties, Phys. Rev. Lett. **120**, 145301 (2018).

[7] F. A. Faber, A. Lindmaa, O. A. von Lilienfeld, and R. Armiento, Machine learning energies of 2 million elpasolite (ABC_2D_6) crystals, Phys. Rev. Lett. **117**, 135502 (2016).

[8] D. Xue, P. V. Balachandran, J. Hogden, J. Theiler, D. Xue, and T. Lookman, Accelerated search for materials with targeted properties by adaptive design, Nat. Commun. **7**, 11241 (2016).

[9] A. Seko, A. Togo, H. Hayashi, K. Tsuda, L. Chaput, and I. Tanaka, Prediction of low-thermal-conductivity compounds with first-principles anharmonic lattice-dynamics calculations and Bayesian optimization, Phys. Rev. Lett. **115**, 205901 (2015).

[10] J. J. Hopfield, Neural networks and physical systems with emergent collective computational abilities, Proc. Natl. Acad. Sci. **79**, 2554 (1982).

[11] J. Hertz, A. Krogh, and R. G. Palmer, *Introduction to the Theory of Neural Computation* (Addison-Wesley, Reading, MA, 1991), 1st ed.

[12] M. Frean, The upstart algorithm: A method for constructing and training feedforward neural networks, Neural Comput. **2**, 198 (1990).

[13] Q. Liu and Y. Wu, in *Encyclopedia of the Sciences of Learning*, edited by N. M. Seel (Springer US, Boston, MA, 2012), p. 3243.

[14] J. Schmidhuber, Deep learning in neural networks: An overview, Neur. Netw. **61**, 85 (2015).

[15] T. K. Ho, Random decision forests, in *Proceedings of 3rd International Conference on Document Analysis and Recognition* (1995), Vol. 1, pp. 278–282.

[16] T. Gilbert, A phenomenological theory of damping in ferromagnetic materials, IEEE Trans. Magn. **40**, 3443 (2004).

[17] W. F. Brown, *Micromagnetics* (Interscience Publishers, New York, 1963).

[18] H. Kronmüller, in *Materials Science and Technology* (John Wiley & Sons, Ltd, 2019), pp. 1–43.

[19] J. F. Herbst, $R_2Fe_{14}B$ materials: Intrinsic properties and technological aspects, Rev. Mod. Phys. **63**, 819 (1991).

[20] A. Aharoni, *Introduction to the Theory of Ferromagnetism* (Oxford University Press, United Kingdom, 2001), 2nd ed.

[21] C. Laplane, E. Z. Cruzeiro, F. Fröwis, P. Goldner, and M. Afzelius, High-precision measurement of the Dzyaloshinsky-Moriya interaction between two rare-earth ions in a solid, Phys. Rev. Lett. **117**, 037203 (2016).

[22] C. Bhandari and D. Paudyal, Giant magnetic and optical anisotropy in cerium-substituted *m*-type strontium hexaferrite driven by 4*f* electrons, Phys. Rev. Appl. **20,** 024016 (2023).

[23] A. Vansteenkiste, J. Leliaert, M. Dvornik, M. Helsen, F. Garcia-Sanchez, and B. Van Waeyenberge, The design and verification of Mumax3, AIP Adv. **4,** 107133 (2014).

[24] J. Leliaert, B. Van de Wiele, A. Vansteenkiste, L. Laurson, G. Durin, L. Dupré, and B. Van Waeyenberge, Current-driven domain wall mobility in polycrystalline permalloy nanowires: A numerical study, J. Appl. Phys. **115,** 233903 (2014).

[25] L. Exl, S. Bance, F. Reichel, T. Schrefl, H. Peter Stimming, and N. J. Mauser, LaBonte's method revisited: An effective steepest descent method for micromagnetic energy minimization, J. Appl. Phys. **115,** 17D118 (2014).

[26] N. Imamura and S. Chikazumi, Determination of exchange stiffness constant using high speed switching of Fe-Ni magnetic thin films, J. Phys. Soc. Jpn. **25,** 125 (1968).

[27] R. A. Ristau, K. Barmak, L. H. Lewis, K. R. Coffey, and J. K. Howard, On the relationship of high coercivity and L1 ordered phase in CoPt and FePt thin films, J. Appl. Phys. **86,** 4527 (1999).

[28] B. C. Sales, B. Saparov, M. A. McGuire, D. J. Singh, and D. S. Parker, Ferromagnetism of Fe_3Sn and alloys, Sci. Rep. **4,** 7024 (2014).

[29] H. Jaballah, W. Bouzidi, R. Fersi, N. Mliki, and L. Bessais, Structural, magnetic and magnetocaloric properties of $(Pr, Sm)_2Fe_{17}$ compound at room temperature, J. Phys. Chem. Solids **161,** 110438 (2022).

[30] Y. Iwama, M. Takeuchi, and M. Iwata, New determination of magnetic anisotropy constants of alnico magnet alloys, J. Phys. Colloq. **32,** C1 (1971).

[31] Y. Liu, J. Song, G. Liu, J. Chen, C. Wang, H. Wang, J. Wang, and X. Zhang, High strength and low coercivity of cobalt with three-dimensional nanoscale stacking faults, Nano Lett. **21,** 6480 (2021).

[32] H. Sato, T. Yoshioka, H. Tsuchiura, Y. Mizuno, K. Koike, K. Takahashi, and H. Kato, Rare-earth moment reduction and local magnetic anisotropy in $Pr_2Fe_{14}B$ and $Tm_2Fe_{14}B$, J. Magn. Magn. Mater. **545,** 168684 (2022).

[33] N. Yu, M. Zhu, L. Song, Y. Fang, K. Song, Q. Wang, and W. Li, Coercivity temperature dependence of Sm_2Co_{17}-type sintered magnets with different cell and cell boundary microchemistry, J. Magn. Magn. Mater. **452,** 272 (2018).

[34] T. Kikuchi, T. Nakamura, T. Yamasaki, M. Nakanishi, T. Fujii, J. Takada, and Y. Ikeda, Magnetic properties of La–Co substituted *M*-type strontium hexaferrites prepared by polymerizable complex method, J. Magn. Magn. Mater. **322,** 2381 (2010).

[35] K. M. U. Rehman, M. Riaz, X. Liu, M. W. Khan, Y. Yang, K. M. Batoo, S. F. Adil, and M. Khan, Magnetic properties of Ce doped *m*-type strontium hexaferrites synthesized by ceramic route, J. Magn. Magn. Mater. **474,** 83 (2019).

[36] P. Wang, X. Wang, L. Qiao, J. Zhang, G. Wang, B. Duan, T. Wang, and F. Li, High-frequency magnetic properties and microwave absorption performance of oxidized Pr_2Co_{17} flakes/epoxy composite in x-band, J. Magn. Magn. Mater. **468,** 193 (2018).

[37] J. Zhang, H. Gao, Y. Yan, X. Bai, F. Su, W. Wang, and X. Du, Morphology and magnetic properties of $CeCo_5$ submicron flakes prepared by surfactant-assisted high-energy ball milling, J. Magn. Magn. Mater. **324,** 3272 (2012).

[38] A. Gabay, X. Hu, and G. Hadjipanayis, Preparation of YCo_5, $PrCo_5$ and $SmCo_5$ anisotropic high-coercivity powders via mechanochemistry, J. Magn. Magn. Mater. **368,** 75 (2014).

[39] Y. Hirayama, A. Panda, T. Ohkubo, and K. Hono, High coercivity $Sm_2Fe_{17}N_3$ submicron size powder prepared by polymerized-complex and reduction–diffusion process, Scr. Mater. **120,** 27 (2016).

[40] J. Fliegans, Coercivity of NdFeB-based sintered permanent magnets: Experimental and numerical approaches, Theses, Université Grenoble Alpes, 2019, https://theses.hal.science/tel-02635105.

[41] Q. Cheng, J. Lin, and M. Su, On synthesis and magnetic properties of $Nd(Fe, Mo, Ti)_{12}Z_x$ $(Z = N, H)$, J. Alloys Compd. **280,** 310 (1998).

[42] S. T. Oyama, ed., *The Chemistry of Transition Metal Carbides and Nitrides* (Springer Dordrecht, Dordrecht, 1996), 1st ed., pp. XXVI, 536.

[43] T. Wu, S. Cao, M. Kou, Y. Xie, G. Ding, S. Guo, B. Zheng, R. Chen, M. Zhong, and A. Yan, Magnetic performance and microstructure of NdFeB sintered magnet by diffusing $Tb_{10}Pr_{90-x}(Cu, Al, Ga)_x$ alloys, J. Alloys Compd. **934,** 167888 (2023).

[44] J. Tsui, K. Strnat, and J. Schweizer, High magnetic coercivity of neodymium- and didymium-cobalt alloys sintered with Pr and Sm additives, APL **21,** 446 (2003).

[45] C. Zhou and F. E. Pinkerton, Magnetic properties of Ce–Nd–Fe–Mo alloys and their nitrides, J. Magn. Magn. Mater. **369,** 127 (2014).

[46] G. Gkouzia, D. Günzing, R. Xie, T. Weßels, A. Kovács, A. T. N'Diaye, M. Major, J. P. Palakkal, R. E. Dunin-Borkowski, H. Wende, H. Zhang, K. Ollefs, and L. Alff, Element-specific study of magnetic anisotropy and hardening in $SmCo_{5-x}Cu_x$ thin films, Inorg. Chem. **62,** 16354 (2023).

[47] K. Suresh, R. Gopalan, A. Singh, G. Bhikshamaiah, V. Chandrasekaran, and K. Hono, Coercivity of $Sm(Co_{0.9}Cu_{0.1})_{4.8}$ melt-spun ribbons, J. Alloys Compd. **436,** 358 (2007).

[48] J. Téllez-Blanco, R. Grössinger, and R. Sato Turtelli, Structure and magnetic properties of $SmCo_{5-x}Cu_x$ alloys, J. Alloys Compd. **281,** 1 (1998).

[49] M. D. Kuz'min, K. P. Skokov, I. Radulov, C. A. Schwöbel, S. Foro, W. Donner, M. Werwiński, J. Rusz, E. Delczeg-Czirjak, and O. Gutfleisch, Magnetic anisotropy of La_2Co_7, J. Appl. Phys. **118,** 053905 (2015).

[50] M. Q. Huang, S. G. Sankar, W. E. Wallace, M. E. McHenry, Q. Chen, and B. M. Ma, Structure and magnetic properties of $RCo_{7-x}Zr_x$ $(R = Y, Gd, Nd, \text{or Ho}, x = 0 - 0.8)$, J. Appl. Phys. **87,** 5305 (2000).

[51] M. T. Onyszczak, T. N. Lamichhane, S. L. Bud'ko, P. C. Canfield, and A. Palasyuk, Structural and magnetic properties of the $CeCo_5$–$CeZn_5$ solid solution and potential improvements upon iron substitution, J. Magn. Magn. Mater. **482,** 192 (2019).

[52] Y. Wong, H. Chang, Y. Lee, W. Chang, C. Chiu, and C. Mo, Coercivity enhancement of thicker sintered NdFeB magnets by grain boundary diffusion with low-melting $Tb_{75-x}Ce_xCu_{25}$ ($x = 0$–45) alloys, J. Magn. Magn. Mater. **515**, 167287 (2020).

[53] W. Silva, N. Ferreira, J. Soares, R. da Silva, and M. Macêdo, Investigation of structural and magnetic properties of nanocrystalline Mn-doped $SrFe_{12}O_{19}$ prepared by proteic sol–gel process, J. Magn. Magn. Mater. **395**, 263 (2015).

[54] S. Katlakunta, S. S. Meena, S. Srinath, M. Bououdina, R. Sandhya, and K. Praveena, Improved magnetic properties of Cr^{3+} doped $SrFe_{12}O_{19}$ synthesized via microwave hydrothermal route, Mater. Res. Bull. **63**, 58 (2015).

[55] S. Chawla, S. Meena, P. Kaur, R. Mudsainiyan, and S. Yusuf, Effect of site preferences on structural and magnetic switching properties of CO-Zr doped strontium hexaferrite $SrCo_xZr_xFe_{(12-2x)}O_{19}$, J. Magn. Magn. Mater. **378**, 84 (2015).

[56] R. Alange, P. P. Khirade, S. D. Birajdar, A. V. Humbe, and K. Jadhav, Structural, magnetic and dielectrical properties of Al–Cr Co-substituted *m*-type barium hexaferrite nanoparticles, J. Mol. Struct. **1106**, 460 (2016).

[57] J. Lee, E. J. Lee, T.-Y. Hwang, J. Kim, and Y.-H. Choa, Anisotropic characteristics and improved magnetic performance of Ca–La–Co-substituted strontium hexaferrite nanomagnets, Sci. Rep. **10**, 15929 (2020).

[58] M. R. Rehman, M. A. Akram, and I. H. Gul, Improved electrical properties of strontium hexaferrite nanoparticles by Co^{2+} substitutions, ACS Omega **7**, 43432 (2022).

[59] K. Lee, Y.-M. Kang, and S.-I. Yoo, Effects of La-Co substitution and post-annealing on the magnetic properties of SrM hexaferrites (2022).

[60] M. L. Ghimire, D. L. Kunwar, J. N. Daha, S. Dipesh Neupane, Sunghyun Yoon, and R. Mishra, Co-doped rare-earth (La, Pr) and Co-Al substituted *m*-type strontium hexaferrite: Structural, magnetic, and mossbauer spectroscopy study, MSA **11**, 474 (2020).

[61] K. Aledealat, B. Aladerah, A. Obeidat, and M. Gharaibeh, First-principles study of electronic structure and magnetic properties of L10-ordered FeNi, FePd, and FePt alloys, Heliyon **7**, e08639 (2021).

[62] L. Luo, N. Anuniwat, N. Dao, Y. Cui, S. A. Wolf, and J. Lu, Magneto-transport and domain wall scattering in epitaxy L1 MnAl thin film, J. Appl. Phys. **119**, 103902 (2016).

[63] R. S. Azis, S. Sulaiman, I. R. Ibrahim, A. Zakaria, J. Hassan, N. N. C. Muda, R. Nazlan, N. M. Saiden, Y. W. Fen, M. S. Mustaffa, and K. A. Matori, Influence of pH adjustment parameter for sol–gel modification on structural, microstructure, and magnetic properties of nanocrystalline strontium ferrite, Nanoscale Res. Lett. **13**, 160 (2018).

[64] Y. He, P. Adler, S. Schneider, I. Soldatov, Q. Mu, H. Borrmann, W. Schnelle, R. Schaefer, B. Rellinghaus, G. H. Fecher, and C. Felser, Intrinsic magnetic properties of a highly anisotropic rare-earth-free Fe_2P-based magnet, Adv. Funct. Mater. **32**, 2107513 (2022).

[65] K. J. Strnat and R. M. Strnat, Rare earth-cobalt permanent magnets, J. Magn. Magn. Mater. **100**, 38 (1991).

[66] A. Kovacs, J. Fischbacher, M. Gusenbauer, H. Oezelt, H. C. Herper, O. Y. Vekilova, P. Nieves, S. Arapan, and T. Schrefl, Computational design of rare-earth reduced permanent magnets, Engineering **6**, 148 (2020).

[67] J. Luo, Y. Xu, and H. Mao, Magnetic and microwave absorption properties of rare earth ions (Sm^{3+}, Er^{3+}) doped strontium ferrite and its nanocomposites with polypyrrole, J. Magn. Magn. Mater. **381**, 365 (2015).

[68] P. Nieves, S. Arapan, J. Maudes-Raedo, R. Marticorena-Sánchez, N. Del Brío, A. Kovacs, C. Echevarria-Bonet, D. Salazar, J. Weischenberg, H. Zhang, O. Vekilova, R. Serrano-López, J. Barandiaran, K. Skokov, O. Gutfleisch, O. Eriksson, H. Herper, T. Schrefl, and S. Cuesta-López, Database of novel magnetic materials for high-performance permanent magnet development, Comput. Mater. Sci. **168**, 188 (2019).

[69] Z. Li, B. Shen, M. Zhang, F. Hu, and J. Sun, Substitution of Ce for Nd in preparing $R_2Fe_{14}B$ nanocrystalline magnets, J. Alloys Compd. **628**, 325 (2015).

[70] M. A. Susner, B. S. Conner, B. I. Saparov, M. A. McGuire, E. J. Crumlin, G. M. Veith, H. Cao, K. V. Shanavas, D. S. Parker, B. C. Chakoumakos, and B. C. Sales, 2Flux growth and characterization of Ce-substituted $Nd_2Fe_{14}B$ single crystals, J. Magn. Magn. Mater. **434**, 1 (2017).

[71] K. Kobayashi, K. Urushibata, T. Matsushita, S. Sakamoto, and S. Suzuki, Magnetic properties and domain structures in Nd–Fe–B sintered magnets with Tb additive reacted and diffused from the sample surface, J. Alloys Compd. **615**, 569 (2014).

[72] S. ying Zhang, Z. gang Sun, H. wei Zhang, B. shan Han, B. gen Shen, F. R. de Boer, and K. H. J. Buschow, Magnetic properties and magnetic-domain structures of nanocrystalline $Sm_2Fe_{14.5}Cu_{0.5}$ Ga_2C_y and $Sm_2Fe_{15}Ga_2C_{1.0}$ ribbons prepared by melt-spinning, J. Phys. D **32**, 2990 (1999).

[73] X. Fan, S. Guo, K. Chen, R. Chen, D. Lee, C. You, and A. Yan, Tuning ce distribution for high performance Nd-Ce-Fe-B sintered magnets, J. Magn. Magn. Mater. **419**, 394 (2016).

[74] B. Zhou, Y. Liu, S. Li, W. Fan, X. Liao, J. He, H. Yu, and Z. Liu, Phase precipitation and magnetic properties of melt-spun ternary $Gd_2Fe_{14}B$ alloy and advantages of gadolinium substitution in $Y_2Fe_{14}B$ alloy, J. Rare Earths **41**, 1058 (2023).

[75] S. Lee, B. Das, and V. Harris, Magnetic structure of single crystal $Tb_2Fe_{14}B$, J. Magn. Magn. Mater. **207**, 137 (1999).

[76] J. Fischbacher, A. Kovacs, H. Oezelt, M. Gusenbauer, D. Suess, and T. Schrefl, Effective uniaxial anisotropy in easy-plane materials through nanostructuring, APL **111**, 192407 (2017).

[77] X. B. Liu and I. C. Nlebedim, Phase stability and coercivity in $La_2Fe_{14}B$ magnet, AIP Adv. **13**, 025211 (2023).

[78] D. Goll, R. Loeffler, J. Herbst, R. Karimi, U. Pflanz, R. Stein, and G. Schneider, High-throughput methods for searching new permanent magnet materials, IEEE Trans. Magn. **50**, 1 (2014).

[79] J.-P. Bick, K. Suzuki, E. P. Gilbert, E. M. Forgan, R. Schweins, P. Lindner, C. Kübel, and A. Michels,

Exchange-stiffness constant of a Nd-Fe-B based nanocomposite determined by magnetic neutron scattering, APL **103**, 122402 (2013).

[80] T. Ohtani, N. Kato, S. Kojima, K. Kojima, Y. Sakamoto, I. Konno, M. Tsukahara, and T. Kubo, Magnetic properties of Mn-Al-C permanent magnet alloys, IEEE Trans. Magn. **13**, 1328 (1977).

[81] E. A. Nesbitt, New Permanent Magnet Materials Containing Rare-Earth Metals, J. Appl. Phys. **40**, 1259 (1969).

[82] N. Inaba and M. Futamoto, Exchange stiffness constants of CoCr-alloy thin films, J. Magn. Magn. Mater. **226–230**, 1014 (2001)., Proceedings of the International Conference on Magnetism (ICM 2000).

[83] T. Ben Ghzaiel, W. Dhaoui, A. Pasko, and F. Mazaleyrat, Effect of non-magnetic and magnetic trivalent ion substitutions on BaM-ferrite properties synthesized by hydrothermal method, J. Alloys Compd. **671**, 245 (2016).

[84] E. H. Frei, S. Shtrikman, and D. Treves, Critical size and nucleation field of ideal ferromagnetic particles, Phys. Rev. **106**, 446 (1957).

[85] G. Herzer, Grain size dependence of coercivity and permeability in nanocrystalline ferromagnets, IEEE Trans. Magn. **26**, 1397 (1990).

[86] R. Skomski and J. Coey, Magnetic anisotropy—How much is enough for a permanent magnet?, Scr. Mater. **112**, 3 (2016).

[87] H. Kronmüller, Theory of nucleation fields in inhomogeneous ferromagnets, Phys. Status Solidi (b) **144**, 385 (1987).

[88] F. E. Pinkerton and C. D. Fuerst, Temperature dependence of coercivity in melt-spun and die upset neodymium-iron-boron, J. Appl. Phys. **67**, 4753 (1990).

[89] J. Herbst and J. Croat, Neodymium-iron-boron permanent magnets, J. Magn. Magn. Mater. **100**, 57 (1991).

[90] R. Alben, J. J. Becker, and M. C. Chi, Random anisotropy in amorphous ferromagnets, J. Appl. Phys. **49**, 1653 (2008).

[91] O. Akdogan, W. Li, B. Balasubramanian, D. J. Sellmyer, and G. C. Hadjipanayis, Effect of exchange interactions on the coercivity of $SmCo_5$ nanoparticles made by cluster beam deposition, Adv. Funct. Mater. **23**, 3262 (2013).

[92] G. Herzer, Soft magnetic nanocrystalline materials, Scr. Mater. **33**, 1741 (1995),, Proceedings of an Acta Metallurgica Meeting on Novel Magnetic Structures and Properties.

[93] R. Fischer, T. Schrefl, H. Kronmüller, and J. Fidler, Grain-size dependence of remanence and coercive field of isotropic nanocrystalline composite permanent magnets, J. Magn. Magn. Mater. **153**, 35 (1996).

[94] R. Ramesh, G. Thomas, and B. M. Ma, Magnetization reversal in nucleation controlled magnets. II. Effect of grain size and size distribution on intrinsic coercivity of Fe-Nd-B magnets, J. Appl. Phys. **64**, 6416 (1988).

[95] S. Bance, B. Seebacher, T. Schrefl, L. Exl, M. Winklhofer, G. Hrkac, G. Zimanyi, T. Shoji, M. Yano, N. Sakuma, M. Ito, A. Kato, and A. Manabe, Grain-size dependent demagnetizing factors in permanent magnets, J. Appl. Phys. **116**, 233903 (2014).

[96] F. Pedregosa, G. Varoquaux, A. Gramfort, V. Michel, B. Thirion, O. Grisel, M. Blondel, P. Prettenhofer, R. Weiss, V. Dubourg, *et al.*, Scikit-learn: Machine learning in python, J. Mach. Learn. Res. **12**, 2825 (2011).

[97] D. P. Kingma and J. Ba, in *3rd International Conference on Learning Representations, ICLR 2015, San Diego, CA, USA, May 7–9, 2015, Conference Track Proceedings*, edited by Y. Bengio and Y. LeCun (2015).

[98] M. Abadi, *et al.*, TensorFlow: Large-scale machine learning on heterogeneous systems (2015), software available from https://www.tensorflow.org/.

[99] F. Chollet, *et al.*, Keras (2015), https://github.com/fchollet/keras.

[100] L. Breiman, J. Friedman, C. J. Stone, and R. Olshen, *Classification and Regression Trees* (Chapman and Hall/CRC, Boca Raton, FL, 1984).

[101] G. Kresse and J. Furthmüller, Efficient iterative schemes for ab initio total-energy calculations using a plane-wave basis set, Phys. Rev. B **54**, 11169 (1996).

[102] G. Kresse and J. Furthmüller, Efficiency of ab-initio total energy calculations for metals and semiconductors using a plane-wave basis set, Comput. Mater. Sci. **6**, 15 (1996).

[103] J. P. Perdew, K. Burke, and M. Ernzerhof, Generalized gradient approximation made simple, Phys. Rev. Lett. **77**, 3865 (1996).

[104] P. E. Blöchl, Projector augmented-wave method, Phys. Rev. B **50**, 17953 (1994).

[105] S. L. Dudarev, G. A. Botton, S. Y. Savrasov, C. J. Humphreys, and A. P. Sutton, Electron-energy-loss spectra and the structural stability of nickel oxide: An LSDA+U study, Phys. Rev. B **57**, 1505 (1998).

[106] O. Isnard, W. B. Yelon, S. Miraglia, and D. Fruchart, Neutron-diffraction study of the insertion scheme of hydrogen in $Nd_2Fe_{14}B$, J. Appl. Phys. **78**, 1892 (1995).

[107] H. Oesterreicher, F. Spada, and C. Abache, Anisotropic and high magnetization rare earth transition metal compounds containing metalloids, Mater. Res. Bull. **19**, 1069 (1984).

[108] V. I. Anisimov, J. Zaanen, and O. K. Andersen, Band theory and Mott insulators: Hubbard U instead of Stoner I, Phys. Rev. B **44**, 943 (1991).

[109] C. Bhandari and D. Paudyal, Giant magnetic and optical anisotropy in cerium-substituted M-type strontium hexaferrite driven by 4*f* electrons, Phys. Rev. Appl. **20**, 024016 (2023).

[110] C. Bhandari, M. E. Flatté, and D. Paudyal, Enhanced magnetic anisotropy in lanthanum M-type hexaferrites by quantum-confined charge transfer, Phys. Rev. Mater. **5**, 094415 (2021).

[111] C. Bhandari and D. Paudyal, Enhancing stability and magnetism of $ThMn_{12}$-type cerium-iron intermetallics by site substitution, Phys. Rev. Res. **4**, 023012 (2022).

[112] M. Sagawa, S. Fujimura, H. Yamamoto, Y. Matsuura, and S. Hirosawa, Magnetic properties of rare-earth-iron-boron permanent magnet materials, J. Appl. Phys. **57**, 4094 (1985).

[113] U. von Barth and L. Hedin, A local exchange-correlation potential for the spin polarized case. I, J. Phys. C: Solid State Phys. **5**, 1629 (1972).

[114] D. Pashov, S. Acharya, W. R. Lambrecht, J. Jackson, K. D. Belashchenko, A. Chantis, F. Jamet, and M. van Schilfgaarde, Questaal: A package of electronic structure

methods based on the linear muffin-tin orbital technique, Comput. Phys. Commun. **249**, 107065 (2020).

[115] M. van Schilfgaarde and V. P. Antropov, First-principles exchange interactions in Fe, Ni, and Co, J. Appl. Phys. **85**, 4827 (1999).

[116] A. Liechtenstein, M. Katsnelson, V. Antropov, and V. Gubanov, Local spin density functional approach to the theory of exchange interactions in ferromagnetic metals and alloys, J. Magn. Magn. Mater. **67**, 65 (1987).

[117] P. Weiss, L'hypothèse du champ moléculaire et la propriété ferromagnétique, J. Phys. Theor. Appl. **6**, 661 (1907).

[118] S. V. Tyablikov, *Methods in the Quantum Theory of Magnetism* (Springer, New York, NY, 2013), 1st ed., pp. XVI, 354.

[119] D. Haskel, J. C. Lang, Z. Islam, A. Cady, G. Srajer, M. van Veenendaal, and P. C. Canfield, Atomic origin of magnetocrystalline anisotropy in $Nd_2Fe_{14}B$, Phys. Rev. Lett. **95**, 217207 (2005).

[120] A. K. Pathak, M. Khan, K. A. Gschneidner Jr., R. W. McCallum, L. Zhou, K. Sun, K. W. Dennis, C. Zhou, F. E. Pinkerton, M. J. Kramer, and V. K. Pecharsky, Cerium: An unlikely replacement of dysprosium in high performance Nd–Fe–B permanent magnets, Adv. Mater. **27**, 2663 (2015).

[121] T. Sasaki, T. Ohkubo, Y. Takada, T. Sato, A. Kato, Y. Kaneko, and K. Hono, Formation of non-ferromagnetic grain boundary phase in a Ga-doped Nd-rich Nd–Fe–B sintered magnet, Scr. Mater. **113**, 218 (2016).

[122] P. Larson, I. I. Mazin, and D. A. Papaconstantopoulos, Calculation of magnetic anisotropy energy in $SmCo_5$, Phys. Rev. B **67**, 214405 (2003).

[123] M. Sakurai, S. Wu, X. Zhao, M. C. Nguyen, C.-Z. Wang, K.-M. Ho, and J. R. Chelikowsky, Magnetocrystalline anisotropy in YCo_5 and $ZrCo_5$ compounds from first-principles real-space pseudopotentials calculations, Phys. Rev. Mater. **2**, 084410 (2018).